

Directly measuring single molecule heterogeneity using force spectroscopy

Michael Hinczewski

Department of Physics, Case Western Reserve University, OH 44106

Changbong Hyeon

Korea Institute for Advanced Study, Seoul 130-722, Korea

D. Thirumalai

Department of Chemistry, The University of Texas at Austin, TX 78712

One of the most intriguing results of single molecule experiments on proteins and nucleic acids is the discovery of functional heterogeneity: the observation that complex cellular machines exhibit multiple, biologically active conformations. The structural differences between these conformations may be subtle, but each distinct state can be remarkably long-lived, with random interconversions between states occurring only at macroscopic timescales, fractions of a second or longer. Though we now have proof of functional heterogeneity in a handful of systems—enzymes, motors, adhesion complexes—identifying and measuring it remains a formidable challenge. Here we show that evidence of this phenomenon is more widespread than previously known, encoded in data collected from some of the most well-established single molecule techniques: AFM or optical tweezer pulling experiments. We present a theoretical procedure for analyzing distributions of rupture/unfolding forces recorded at different pulling speeds. This results in a single parameter, quantifying the degree of heterogeneity, and also leads to bounds on the equilibration and conformational interconversion timescales. Surveying ten published datasets, we find heterogeneity in five of them, all with interconversion rates slower than 10 s^{-1} . Moreover, we identify two systems where additional data at realizable pulling velocities is likely to find a theoretically predicted, but so far unobserved cross-over regime between heterogeneous and non-heterogeneous behavior. The significance of this regime is that it will allow far more precise estimates of the slow conformational switching times, one of the least understood aspects of functional heterogeneity.

INTRODUCTION

One of the great problems in modern biology is to understand how the intrinsic diversity of cellular behaviors is shaped by factors outside of the genome. The causes of this heterogeneity are spread across multiple scales, from noise in biochemical reaction networks through epigenetic mechanisms like DNA methylation and histone modification [1]. It might be natural to expect heterogeneity at the cellular level because of the bewildering array of time and length scales associated with the molecules of life that govern cell function. Surprisingly, even at the level of individual biomolecules, diversity in functional properties like rates of enzymatic catalysis [2–5] or receptor-ligand binding [6, 7] can occur. This diversity arises from the presence of many distinct functional states in the free energy landscape, which correspond to long-lived active conformations of the biomolecule. Though the reigning paradigm in proteins and nucleic acids has been a single, folded native structure, well separated in free energy from any other conformations, possibilities about rugged landscapes with multiple native states have been explored for a long time [8–15]. Yet only with the revolutionary advances in single molecule experimental techniques in recent years have we been able to gather direct evidence of functional heterogeneity, in systems ranging from protein enzymes [2–4] and nucleic acids [5, 16, 17], to molecular motors [18] and cell adhesion complexes [6, 7]. As research inevitably moves

toward larger macromolecular systems, the examples of functional heterogeneity will only multiply. We thus need to develop theories that can deduce aspects of the hidden kinetic network of states underlying the single molecule experimental data [19], allowing us to quantify the nature and extent of the heterogeneity.

The focus in this study is single molecule force spectroscopy, conducted either by AFM or optical tweezers, which constitutes an extensive experimental literature over the last two decades. Our contention is that evidence of heterogeneity is widespread in this literature, but has gone largely unnoticed, since researchers (with a few exceptions, discussed below [20–23]) did not recognize the markers in their data that indicated heterogeneous behavior. To remedy this situation, we introduce a universal approach to analyzing distributions of rupture/unfolding forces collected in pulling experiments, which yields a single non-dimensional parameter $\Delta \geq 0$. The magnitude of Δ characterizes the extent of the disorder in the underlying ensemble, the ruggedness of the free energy landscape. Moreover, our method provides a way of estimating bounds on key timescales, describing both the fast local equilibration in each well (distinct system state) of our rugged landscape, and the slow interconversion between the various wells. After verifying the validity of our approach using synthetic data generated from a heterogeneous model system, we survey ten experimental datasets, comprising a diverse set of biomolecular systems from simple DNA oligomers to large complexes of

proteins and nucleic acids. The largest values of Δ in our survey, indicating the strongest heterogeneity, come from systems involving nucleic acids alone or protein/nucleic acid interactions, supporting the hypothesis that nucleic acid free energy landscapes are generally more rugged than those involving only proteins [24]. Our theory thus provides a powerful new analytical tool, for the first time allowing a broad comparison of functional heterogeneity among different biomolecules through a common experimental protocol.

THEORY

Force spectroscopy for a pure, adiabatic system: As a starting point, consider a generic free energy landscape for a biomolecular system with a single functional state (Fig. 1A) subject to an increasing time-dependent external force $f(t)$. For a molecular complex, the functional basin of attraction in the landscape would correspond to an ensemble of bound conformations with similar energies, which we label N. For the case of single molecule folding, this would be the unique native ensemble. The force is applied through an experimental apparatus like an AFM or optical tweezer, typically connected to the biomolecule through protein or nucleic acid linkers of known stiffness. The apparatus is pulled at a constant velocity v , leading to a force ramp with slope $df/dt = \omega_s(f)v$, where $\omega_s(f)$ is the effective stiffness of the setup (linkers plus the AFM cantilever or optical trap). This $\omega_s(f)$ may in general depend on the force, particularly for the AFM setup, where the cantilever stiffness is often comparable to or greater than that of the molecular construct. So we also define a characteristic stiffness \bar{k}_s which we set to the mean $\omega_s(f)$ over the range of forces probed in the experiment (though the precise value of \bar{k}_s is not important). This allows us to introduce a characteristic force loading rate r proportional to the velocity, $r = \bar{k}_s v$.

If at time $t = 0$ the system starts in N, the force ramp tilts the landscape along the extension coordinate. If we model the conformational dynamics of the system as diffusion within this landscape, the tilting eventually leads to a transition out of N, associated with unbinding of the complex or unfolding of the molecule (an ensemble of states we call U). We let $\Sigma_r(t)$ be the survival probability for loading rate r , in other words the probability that the transition to U has not occurred by time t . The distribution of first rupture times is then $-d\Sigma_r/dt$, and the mean rupture rate $\bar{k}(r)$ is just the inverse of the average rupture time,

$$\bar{k}(r) = \left[\int_0^\infty dt t \left(-\frac{d\Sigma_r}{dt} \right) \right]^{-1} = \left[\int_0^\infty dt \Sigma_r(t) \right]^{-1}, \quad (1)$$

where we have used integration by parts and assumed that rupture always occurs if we wait long enough, $\Sigma(\infty) = 0$.

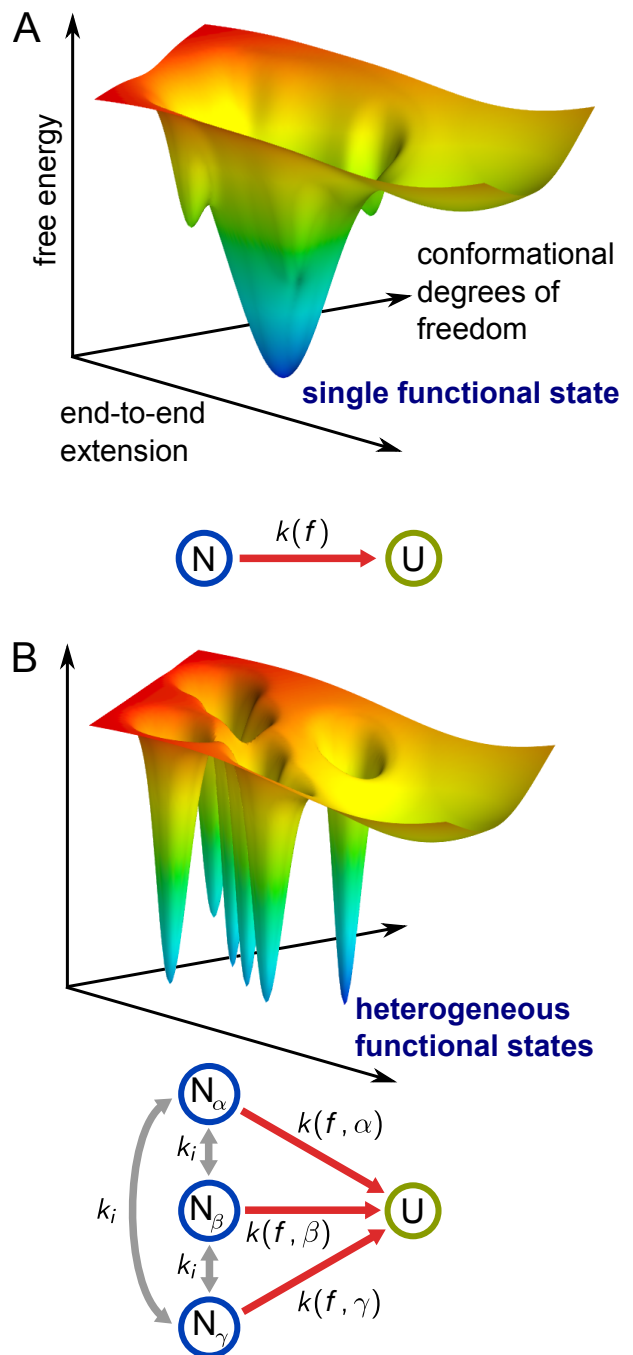


FIG. 1. A) Schematic biomolecular free energy landscape with a single functional state, N, corresponding to an ensemble of folded/bound conformations. Under an adiabatically increasing external force $f(t)$, there is an instantaneous rupture rate $k(f(t))$ describing transitions between N and the unfolded/unbound ensemble U. B) Schematic free energy landscape of a heterogeneous system with multiple functional states. Each functional ensemble N_α will have a state-dependent adiabatic rupture rate $k(f, \alpha)$. Assuming the states are roughly equally probable in equilibrium, there will be a single overall rate k_i for interconversion between the various states.

The behavior of $\Sigma_r(t)$ at different r depends on how $\bar{k}(r)$ compares to two other intrinsic rates. The first is the equilibration rate k_{eq} in the N well, or how quickly the system samples the configurations of the functional ensemble. For a single, smooth well with mean curvature ω_0 and a diffusion constant D , this rate is on the order of $k_{\text{eq}} \sim \beta\omega_0 D$, where $\beta = 1/k_B T$. The second is a critical rate $k_c(r) = r/f_c$, which describes how quickly the force reaches a critical force scale for rupture $f_c \sim G^\ddagger/x^\ddagger$. Here G^\ddagger is the energy scale of the barrier that needs to be overcome for the N to U transition at zero force, and x^\ddagger the extension difference between the N well minimum and the transition state. For $f \gtrsim f_c$ the landscape is tilted sufficiently that the barrier becomes insignificant, and rupture occurs quickly (on a diffusion-limited time scale). If $k_c(r) \ll \bar{k}(r) \ll k_{\text{eq}}$, the system is in the adiabatic regime. The force ramp is sufficiently slow that rupture occurs before the critical force is reached, and equilibration is fast enough that the system can reach quasi-equilibrium at the instantaneous value of the force $f(t)$ at all times t before the rupture.

If the adiabatic condition is satisfied, the survival probability $\Sigma_r(t)$ obeys the kinetic equation $d\Sigma_r(t)/dt = -k(f(t))\Sigma_r(t)$, where $k(f)$ is the rupture rate at constant force f . Since $f(t)$ is a monotonically increasing function of t , we can change variables from t to $f(t)$ [25], and solve for $\Sigma_r(f)$, the probability that the system does not rupture before the force value f is reached:

$$\Sigma_r(f) = \exp\left(-\frac{1}{r} \int_0^f df' \frac{\bar{k}_s k(f')}{\omega_s(f')}\right). \quad (2)$$

Interestingly, the integral inside the exponential is independent of the loading rate r . Hence for a system pulled from a single native ensemble, we can calculate the following quantity from experimental trajectories at different r ,

$$\Omega_r(f) \equiv -r \log \Sigma_r(f), \quad (3)$$

and the results should collapse onto a single master curve for all r in the adiabatic regime. When r is sufficiently large that $\bar{k}(r) < k_c(r)$ or $\bar{k}(r) > k_{\text{eq}}$, the assumption of quasi-equilibrium on a slowly changing energy landscape breaks down, and Eq. (2) no longer holds. For this fast, non-adiabatic case [26, 27] we should find that $\Omega_r(f)$ varies with r , as we will explore later in more detail.

Force spectroscopy for a heterogeneous, adiabatic system: In a pioneering series of studies, Raible and collaborators analyzed force ramp experiments for the regulatory protein ExpG unbinding from a DNA fragment [20–22]. Plotting $\Omega_r(f)$ (the data reproduced in Fig. 6D), they did not find any collapse, as might be surmised from Eq. 3. This was not an artifact due to non-adiabaticity (violation of the inequality $k_c(r) \ll \bar{k}(r) \ll k_{\text{eq}}$), since the absence of collapse becomes even more pronounced at small loading rates, further into the adiabatic territory

where collapse should be observed. They correctly surmised that the cause of this divergence is heterogeneity in the ensemble of states in the protein-DNA complex.

To understand the behavior of $\Omega_r(f)$ in a heterogeneous system, let us consider the effects of a force ramp on a biomolecular free energy landscape with multiple functional states (Fig. 1B). Our goal is to use $\Omega_r(f)$, derived from experimental pulling trajectories, to quantify the extent of the heterogeneity and extract information about the underlying conformational dynamics. The functional states are distinct basins of attraction in the landscape, corresponding to distinct functional ensembles which we label N_α for state α . We assume the minimum energy in each well and their overall dimensions are comparable, so that the equilibrium probabilities p_α^{eq} of the various states are of the same order. In this case if $\alpha \neq \alpha'$, the transition rates $k_{\alpha \rightarrow \alpha'}$ and $k_{\alpha' \rightarrow \alpha}$ are also similar from detailed balance, $k_{\alpha \rightarrow \alpha'}/k_{\alpha' \rightarrow \alpha} = p_{\alpha'}^{\text{eq}}/p_\alpha^{\text{eq}} \sim O(1)$. Hence we can introduce an overall scale for the interconversion rate between the different states, k_i , such that $k_{\alpha \rightarrow \alpha'} \sim O(k_i)$ for any $\alpha \neq \alpha'$. Thus we now have two intrinsic time scales: k_{eq} for equilibration within a single N_α , and k_i for transitions between distinct N_α 's, where typically $k_i < k_{\text{eq}}$.

The experimental setup is the same as above, with a loading rate r , and a corresponding mean rupture rate $\bar{k}(r)$ for reaching the U ensemble. We can identify three dynamical regimes, based on the magnitude of k_i . In the first regime, interconversion is slow, with $k_i \ll \bar{k}(r)$. In the second regime, k_i is comparable to $\bar{k}(r)$. In fact, as we will discuss later in more detail, we will be particularly interested in the cross-over scenario where $k_i \geq \bar{k}(r)$ for some subset of the r values in the experiment, but $k_i < \bar{k}(r)$ for the remainder. If this second regime is identified in an experiment, it provides a way to estimate the scale of k_i . Finally, in the third regime, the barriers between the N_α basins of attraction are small, such that $k_i \gg \bar{k}(r)$, and the system can sample all the states before rupture. Qualitatively, this scenario is indistinguishable from the case of a system with a single native basin of attraction, with k_i taking the role of k_{eq} as the rate scale for overall equilibration in the landscape. Since the first regime is simpler to treat mathematically than the second regime, we will initially focus on a theory to describe the first regime and identify its signatures in experimental data. Assessing the validity of this theory in experiments will turn out to be a useful criterion for distinguishing between the first, second, and third regimes, and thus putting bounds on k_i . This byproduct of our theory is of considerable importance because it is *a priori* very difficult to estimate k_i .

To begin, consider adiabatic pulling where k_i is the slowest rate in the system, $k_i \ll k_c(r) \ll \bar{k}(r) \ll k_{\text{eq}}$. On the time scale of pulling and rupture, the system is effectively trapped in a heterogeneous array of states: if we start a pulling trajectory in state α , the system will remain in that state until rupture. The rupture rate at constant force, $k(f, \alpha)$ will in general depend on the

state, and the ensemble of molecules from which we pull will be characterized by a set of initial state probabilities p_α . If k_i is extremely small, such that the system cannot interconvert even on the macroscopic time scales of experimental preparation, p_α may be different from p_α^{eq} , since we are not guaranteed to draw from an equilibrium distribution across the entire landscape. This distinction is not important for the analysis below. In fact, our approach also works when $k_i = 0$, corresponding to the quenched disorder limit, as seen for example in an ensemble of molecules with covalent chemical differences.

The analogue of Eq. 2 for the survival probability $\Sigma_r(f)$ during adiabatic pulling in a heterogeneous system with small k_i is

$$\Sigma_r(f) = \left\langle \exp \left(-\frac{1}{r} \int_0^f df' \frac{\bar{k}_s k(f', \alpha)}{\omega_s(f')} \right) \right\rangle, \quad (4)$$

where the brackets denote an average over the initial ensemble of states, $\langle O(\alpha) \rangle \equiv \sum_\alpha p_\alpha O(\alpha)$ for any quantity $O(\alpha)$. The associated $\Omega_r(f)$ from Eq. (3) can be expressed through a cumulant expansion in terms of the integrand $I(f, \alpha) \equiv \int_0^f df' \bar{k}_s k(f', \alpha) / \omega_s(f')$ as follows:

$$\begin{aligned} \Omega_r(f) &= - \sum_{n=1}^{\infty} (-1)^n \frac{\kappa_n(f)}{n! r^{n-1}}, \\ \kappa_n(f) &\equiv \left. \frac{\partial^n}{\partial \lambda^n} \log \langle e^{\lambda I(f, \alpha)} \rangle \right|_{\lambda=0}. \end{aligned} \quad (5)$$

The first two cumulants are $\kappa_1(f) = \langle I(f, \alpha) \rangle$ and $\kappa_2(f) = \langle I^2(f, \alpha) \rangle - \langle I(f, \alpha) \rangle^2$. In the absence of heterogeneity, all cumulants $\kappa_n(f)$ with $n > 1$ are exactly zero. For a small degree of heterogeneity, or equivalently for sufficiently fast loading rates r , the main contribution to the expansion is from the $n = 1$ and $n = 2$ terms. For the case of fast r we assume that we are still within the adiabatic regime, where $k_c(r) \ll \bar{k}(r)$, which turns out to be valid even for the largest loading rates in the experimental studies discussed below. In this scenario, where the $n > 2$ contributions are negligible, $\Omega_r(f)$ can be approximated as

$$\Omega_r(f) \approx \frac{r}{\Delta(f)} \log \left(1 + \frac{\kappa_1(f) \Delta(f)}{r} \right) \quad (6)$$

where $\Delta(f) \equiv \kappa_2(f) / \kappa_1^2(f) \geq 0$ is a dimensionless measure of the ensemble heterogeneity. For a pure system, $\Delta(f) \rightarrow 0$, giving $\Omega_r(f) \rightarrow \kappa_1(f)$, independent of r . Eq. (6) agrees with the expansion in Eq. (5) up to order $n = 2$, and also has the nice property that it satisfies the inequality $\Omega_r(f) \leq \kappa_1(f)$, just like the exact form. The latter inequality follows from the definition of $\Sigma_r(f)$ in Eq. (4) and Jensen's inequality, $\Sigma_r(f) \geq \exp(-\kappa_1(f)/r)$.

Implementing the model on experimental data: So far the discussion has been completely general, but to fit Eq. (6) to experimental data we need specific forms for $\Delta(f)$ and $\kappa_1(f)$. The minimal physically sensible approx-

imation, with the smallest number of unknown parameters, supplements Eq. (6) with the assumptions,

$$\Delta(f) = \Delta, \quad \kappa_1(f) = \frac{k_0}{\beta x^\ddagger} \left(e^{\beta f x^\ddagger} - 1 \right). \quad (7)$$

The constants Δ , k_0 , and x^\ddagger are fitting parameters. This presumes that $\Delta(f)$ changes little over the range of forces in the data, and $\kappa_1(f)$ has the same mathematical form as in a pure Bell model with an escape rate $k(f) = k_0 e^{\beta f x^\ddagger}$ and $\omega_s(f) = \bar{\omega}_s$, where k_0 is the escape rate at zero force and x^\ddagger the distance to the transition state. For a heterogeneous system, the parameters k_0 and x^\ddagger no longer have this simple interpretation, but we can still treat them as effective Bell values, averaged over the ensemble, with Δ measuring the overall scale of the heterogeneity. Eq. (6), together with the three-parameter approximation of Eq. (7), provides remarkably accurate fits to all the heterogeneous experimental data sets we have encountered in the literature. As will be seen below, it is capable of simultaneously fitting $\Omega_r(f)$ data for loading rates r spanning nearly two orders of magnitude.

Though we focus on $\Omega_r(f)$ as the main experimental quantity of interest, Eqs. (6)-(7) can also be used to derive a closed form expression for the probability distribution of rupture forces, $p_r(f) = -d\Sigma_r(f)/df = -(d/df) \exp(-\Omega_r(f)/r)$, at loading rate r :

$$p_r(f) = \frac{k_0 e^{\beta f x^\ddagger}}{r} \left(1 + \frac{\Delta k_0 (e^{\beta f x^\ddagger} - 1)}{\beta r x^\ddagger} \right)^{-\frac{\Delta+1}{\Delta}}. \quad (8)$$

In the limit of no heterogeneity, $\Delta \rightarrow 0$, this distribution reduces to the one predicted for a Bell model under a constant loading rate [25]. The theoretical form for $p_r(f)$ also allows us to carry out a relative likelihood analysis on the experimental data, to verify that Δ is indeed a robust indicator of heterogeneity. As detailed in SI Sec. 6, we found that experimental distributions $p_r(f)$ corresponding to systems with nonzero Δ were far more likely to be described by the heterogeneous theory in Eq. (8) than a pure model with the same number of parameters. We surmise that if analysis of experimental data using our theory indicates that $\Delta \neq 0$ then it is highly probable that any single state model is insufficient to describe the system, and a multiple state description is needed.

To verify that our analysis and conclusions would not change substantially if the assumptions of the minimal model were relaxed, we have also tested two generalized versions of the model: one using the Dudko-Hummer-Szabo [28] instead of the Bell form for the escape rate in $\kappa_1(f)$, and the other allowing $\Delta(f)$ to vary linearly with f across the force range. Both extensions have four instead of three fitting parameters, but the heterogeneity results for the experimental systems we analyzed are completely consistent with those obtained using the minimal model (see Supplementary Information (SI) Sec. 1 for details). These results demonstrate that if the need arises in future experimental contexts, the theory leading to Eq. (6) is quite general, and can be tailored by

choosing suitable expressions for $\kappa_1(f)$ and $\Delta(f)$ that go beyond the minimal model of Eq. (7).

The theory described up to now applies only to the first dynamical regime, where $k_i \ll \bar{k}(r)$. However the cases where k_i is larger than some or all of the $\bar{k}(r)$, and the theory partially or completely fails, turn out to be very informative as well. To understand these points, it is easier to discuss the theory in the context of a concrete physical model for heterogeneity, which we introduce in the next section.

RESULTS AND DISCUSSION

Fluctuating Barrier Location (FBL) model: Before turning to experimental data, we verify that the Δ parameter extracted from the fitting of $\Omega_r(f)$ curves using Eqs. (6)-(7) is a meaningful measure of heterogeneity. To do this, we will generate synthetic rupture data from a heterogeneous model system. The FBL model, illustrated in Fig. 2A, consists of a reaction coordinate x whose dynamics are described by diffusion with constant D along a parabolic free energy $U(x) = (1/2)\omega_0 x^2$ for $x \leq x^\ddagger$. Rupture occurs if x exceeds the transition distance x^\ddagger . To mimic dynamic heterogeneity, the value of x^\ddagger changes at random intervals, governed by a Poisson process with an interconversion rate k_i . At every switching event, a new value of x^\ddagger is drawn from a Gaussian probability distribution $P(x^\ddagger) = \exp(-(x^\ddagger - x_0^\ddagger)^2/2\sigma^2)/\sqrt{2\pi\sigma^2}$ centered at x_0^\ddagger with standard deviation σ , and diffusion continues if x is less than the transition distance. At time $t = 0$, when the applied force ramp $f(t) = rt$ begins, we assume the initial ensemble of systems all start at $x = 0$ with x^\ddagger values distributed according to $P(x^\ddagger)$. Survival probabilities $\Sigma_r(f)$ are computed from numerical simulations of the diffusive process, with about 3×10^4 rupture events collected for each parameter set (see the SI Sec. 2 for additional details). The simplicity of the model, where one parameter, σ , controls the degree of heterogeneity, and another, k_i , the interconversion dynamics, allows us to explore the behavior of $\Sigma_r(f)$, and hence $\Omega_r(f)$, over a broad range of disorder and intrinsic time scales.

The circles in Fig. 2C-D show simulation results for $\Omega_r(f)$ between $f = 0 - 50$ pN, plotted on a logarithmic scale, with each color denoting a different ramp rate in the range $r = 200 - 10000$ pN/s. The model parameters are $D = 100$ nm²/s, $\omega_0 = 400$ $k_B T$ /nm², $x_0^\ddagger = 0.2$ nm, $\sigma = 0 - 0.05$ nm, $k_i = 0 - 10^4$ s⁻¹, which give a variety of $\Omega_r(f)$ curves of comparable magnitude over similar force scales to the experimental data discussed below. Fig. 2C shows results for quenched disorder ($k_i = 0$) at different σ , while Fig. 2D shows results for varying k_i at fixed $\sigma = 0.05$ nm. For a given choice k_i and σ , we fit the analytical form of Eq. (6)-(7) simultaneously to the six $\Omega_r(f)$ curves at different r , with the best-fit model plotted as solid lines in Fig. 2C-D. This fitting yields

values for Δ , k_0 , and x^\ddagger in each case. The variation of Δ with σ and k_i is plotted as a heat map in Fig. 2B.

Let us first consider the quenched disorder results (Fig. 2C and the left column of Fig. 2B). By definition, since $k_i = 0$, the system ensemble is permanently frozen in a heterogeneous array of different states with different values of x^\ddagger . Moreover, the adiabatic assumptions also hold, as can be seen in the insets to Fig. 2C. These show the mean rupture rate $\bar{k}(r)$ for different r (circles) compared to k_{eq} (dotted line) and $k_c(r)$ (dashed line). For all the r values analyzed, $k_c(r) < \bar{k}(r) \ll k_{\text{eq}}$, so adiabaticity should approximately hold. Thus the assumptions leading to Eqs. (6)-(7) are valid, and indeed the analytical form provides an excellent fit to the simulation data. Though the theory is by construction most accurate in the limit of fast (but still adiabatic) r , it still quantitatively describes the results for r spanning two orders of magnitude. Only small discrepancies start to appear at the slowest loading rates. For the pure system limit ($\sigma = 0$) the best-fit value of Δ is also zero, with all the $\Omega_r(f)$ curves collapsing on one another. Δ progressively increases with σ , growing roughly proportional to the width of the disorder distribution. The greater the heterogeneity, the more pronounced the separation between the $\Omega_r(f)$ curves at various r .

The results in Fig. 2D are obtained by keeping the extent of heterogeneity fixed at a large level ($\sigma = 0.05$ nm) and allows interconversion, increasing k_i from 10 to 10^3 s⁻¹. So long as $\bar{k}(r) \gg k_i$, the system is unlikely to interconvert on the time scale of rupture, and we see distinct, non-collapsed $\Omega_r(f)$ curves. But as k_i increases and overtakes $\bar{k}(r)$, starting from the smallest values of r where $\bar{k}(r)$ has the smallest magnitude, the $\Omega_r(f)$ curves begin to collapse on one another. This leads to increasing discrepancies between the data and the theoretical fit, since the assumptions justifying the theory break down when $\bar{k}(r) < k_i$. Eventually, once k_i is greater than all the $\bar{k}(r)$, there is total collapse of the $\Omega_r(f)$ curves (bottom panel of Fig. 2D). Frequent interconversion between the different states of the system before rupture averages out the heterogeneity, making the results indistinguishable from a pure system. In this limit the ensemble of functional states acts effectively like a single functional basin of attraction, with multiple distinct pathways to rupture. Though multiple pathways between a pair of states can be considered to be another manifestation of heterogeneity, they are not in themselves sufficient to lead to non-collapse of the $\Omega_r(f)$ curves, as we discuss in more detail in SI Sec. 3. To see anything but complete collapse of the $\Omega_r(f)$ curves in the adiabatic regime requires a small enough interconversion rate k_i , slower than the mean rupture rates $\bar{k}(r)$ for at least some subset of the r values.

Dynamical regimes and extraction of bounds on time scales of internal dynamics: Interestingly, it is precisely the discrepancy in the theoretical fits with increasing k_i that points the way to one of the most valuable features of our approach. Not only can we measure heterogeneity,

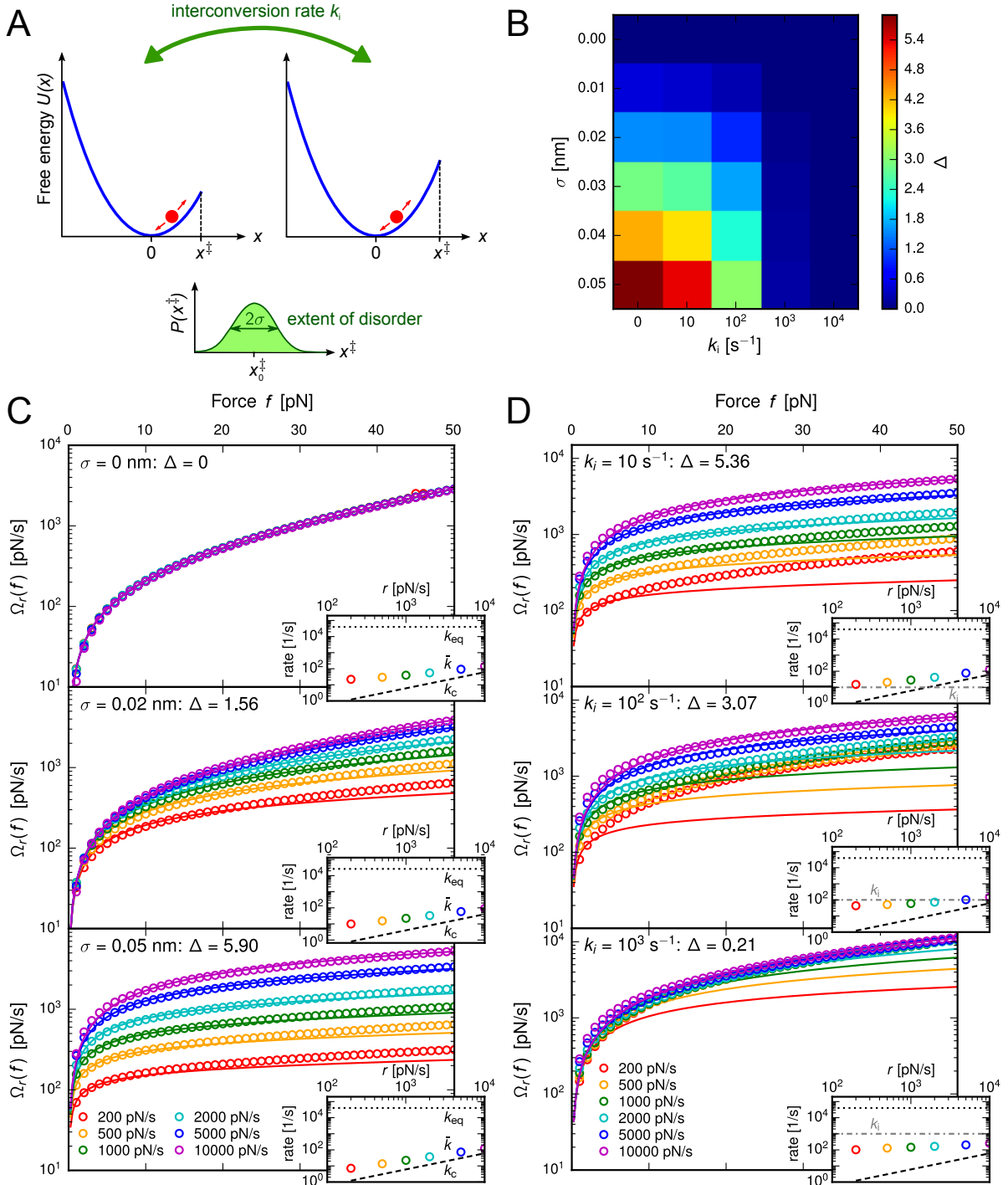


FIG. 2. Analysis of the FBL heterogeneous model system. A) Two different free energy wells, corresponding to distinct states, characterized by different transition distances to rupture, x^\ddagger and $(x^\ddagger)'$. The system switches to a new value of x^\ddagger , drawn from a Gaussian distribution centered at x_0^\ddagger with standard deviation σ , with rate k_i . B) Heat map of Δ as it varies with σ and k_i , extracted from fitting the theory of Eqs. (6)-(7) to numerical simulation results of $\Omega_r(f)$ for the model system. The parameters are: $D = 100 \text{ nm}^2/\text{s}$, $\omega_0 = 400 k_B T/\text{nm}^2$, $x_0^\ddagger = 0.2 \text{ nm}$, $\sigma = 0 - 0.05 \text{ nm}$, $k_i = 0 - 10^4 \text{ s}^{-1}$. C-D) Sample simulation results $\Omega_r(f)$ (circles) on a logarithmic scale, with each color denoting a different loading rate r . The panels show different combinations of k_i and σ , with the plots in C illustrating the case of quenched disorder ($k_i = 0$) for increasing σ , and D showing increasing k_i for fixed $\sigma = 0.05$. The theoretical best-fit curves are drawn as solid curves, and the resulting Δ value is listed in each plot. The insets show the mean rupture rate $\bar{k}(r)$ (circles) as a function of r compared to k_{eq} (dotted line), $k_c(r)$ (dashed line), and k_i (dash-dotted line).

but also infer information about the time scales of conformational dynamics. Note first that the best-fit values of Δ track the disappearance of heterogeneity, monotonically decreasing from $\Delta = 5.90$ at $\sigma = 0.05$, $k_i = 0$ s^{-1} , to $\Delta = 0.21$ at $\sigma = 0.05$, $k_i = 10^3$ s^{-1} . It is clear however that as k_i increases and dynamical disorder becomes more prominent, a single overall value of Δ is an imperfect description of the dynamics. We can get a more fine-grained picture by looking at Δ calculated from smaller subsets of the data, and how it varies with the mean time scale of rupture \bar{k} . To do this let us take $\Omega_r(f)$ curves from two consecutive loading rates (r_1, r_2) , fit Eq. (6)-(7), and calculate the resulting value of Δ , which we will call the ‘‘pair’’ parameter $\Delta_p(r_1, r_2)$. For example, if our total data set consists of six loading rates $r = 200, 500, 1000, 2000, 5000, 10000$ pN/s, we first do this for $(r_1, r_2) = (200, 500)$ pN/s, then $(500, 1000)$ pN/s, and so on, to get five different results for $\Delta_p(r_1, r_2)$. The advantage of this approach is that each Δ_p corresponds to a much smaller range of rupture time scales than what is covered by the entire data set. In Fig. 3A we plot Δ_p for $\sigma = 0.05$, $k_i = 0, 10, 10^2, 10^3$ s^{-1} . The x -axis coordinate is the smaller mean rupture rate of the pair, $\bar{k} = \min(\bar{k}(r_1), \bar{k}(r_2))$.

The behavior of Δ_p in Fig. 3A allows us to identify three different behaviors, corresponding to the three dynamical regimes discussed in the Theory section:

1. *Non-collapse (NC)*: Here all the $\Delta_p(r_1, r_2) \geq 1$, and $\Delta_p(r_1, r_2)$ for any pair of (r_1, r_2) is approximately the same as Δ calculated from the entire data set. We see this in the $k_i = 0$ s^{-1} case in Fig. 3A, where for comparison the value of Δ over the whole set is marked by a horizontal dashed line. The corresponding $\Omega_r(f)$ curves are in the bottom panel of Fig. 2C. The agreement between $\Delta_p(r_1, r_2)$ and Δ is a consistency check for the theory, and implies that the underlying assumptions are valid, namely $k_i < \bar{k}(r)$ and $k_{eq} > \bar{k}(r)$ for all r in the data set. From this we can conclude that the minimum value of $\bar{k}(r)$ among all the loading rates r used in the experiment gives us an upper bound on k_i . Similarly the maximum value of $\bar{k}(r)$ over all r gives a lower bound on k_{eq} . For $k_i = 10$ s^{-1} in Fig. 3A, we see what happens as k_i approaches the time scale of $\bar{k}(r)$. We are still in the NC regime, since $\Delta_p \geq 1$ and k_i (vertical dotted line) is smaller than any of the $\bar{k}(r)$. But k_i is now sufficiently close to $\bar{k}(r = 200$ pN/s) that $\Delta_p(200, 500)$ (the leftmost point) is smaller than the rest of the Δ_p , which lie at faster rupture timescales relatively unaffected by k_i .
2. *Partial collapse (PC)*: $\Delta_p(r_1, r_2) \geq 1$ for the largest values of (r_1, r_2) , but for small loading rates $\Delta_p(r_1, r_2) \ll 1$. This occurs in the $k_i = 10^2$ s^{-1} results in Fig. 3A. In this regime the system is adiabatic, $k_{eq} > \bar{k}(r)$, but now k_i falls between the smallest and largest values of $\bar{k}(r)$. In the $k_i = 10^2$

s^{-1} case, the variation in Δ_p is a reflection of the degree of overlap in the $\Omega_r(f)$ curves (middle panel of Fig. 2D). The $(r_1, r_2) = (5000, 10000)$ pN/s pair (blue and purple $\Omega_r(f)$ circles) are clearly separated, corresponding to $\Delta_p \geq 1$ and the fact that $k_i \lesssim \bar{k}(r_1), \bar{k}(r_2)$. The $(200, 500)$ pN/s pair (red and orange circles) are nearly overlapping, corresponding to $\Delta_p \ll 1$, and $k_i > \bar{k}(r_1), \bar{k}(r_2)$. The PC regime thus provides the best case scenario for directly estimating k_i from the data, since we can bound k_i from above and below, and we know k_i will roughly coincide with the \bar{k} where $\Delta_p(r_1, r_2) \sim 1$.

3. *Total collapse (TC)*: $\Delta_p(r_1, r_2) \ll 1$ for the all (r_1, r_2) in the data set. This is illustrated by the $k_i = 1000$ s^{-1} case in Fig. 3A, corresponding to the $\Omega_r(f)$ curves in the bottom panel of Fig. 2D. Δ_p values close to zero translate into near total overlap of the $\Omega_r(f)$ results. This regime requires adiabaticity, $k_{eq} > k(r)$, and if there is any heterogeneity in the system, the interconversion between states has to be fast, $k_i > \bar{k}(r)$. Thus the maximum value of $\bar{k}(r)$ over all r gives a lower bound on both k_i and k_{eq} .

To summarize, we can use the magnitude of the heterogeneity parameters (Δ or Δ_p depending on whether we look at the whole data set or pairs of ramp rates) to make specific inferences about the nature of the biomolecular free energy landscape. $\Delta \gg 1$ (large disorder) in an experimental data set implies the following facts: there is an ensemble of folded/intact states in the system, these states have substantially different force-dependent rates of rupture, and the system will only rarely switch from one state to another before rupture occurs. A small but finite Δ in the range $0 \ll \Delta \lesssim 1$ (low disorder) indicates that heterogeneity is still present, but one or both of the following are true: the interconversion rate k_i is comparable to the mean rupture rates, so heterogeneity is partially averaged out due to transitions between states, or the differences in rupture rate functions between states are small. Finding $\Delta \approx 0$ (no disorder) indicates that either there is no heterogeneity (a single native state) or that k_i is so large that the ensemble of native states behaves effectively like a single state.

Ruling out non-adiabatic artifacts: One important question about the usefulness of the theory remains: what about situations where the loading rate r is sufficiently fast that the adiabatic assumption $k_c(r) \ll \bar{k}(r) \ll k_{eq}$ breaks down? As mentioned above, $\Omega_r(f)$ in this case will not collapse onto a single master curve independent of r , regardless of the presence of underlying heterogeneity in the system. Since the experimentalist has no direct way of measuring k_{eq} or $k_c(r)$, it is not *a priori* clear whether a given loading rate r is slow enough for adiabaticity to hold. Can the theory in Eqs. (6)-(7) fit a pure system over a range of non-adiabatic r , and yield a non-zero fitted value of Δ that would incorrectly

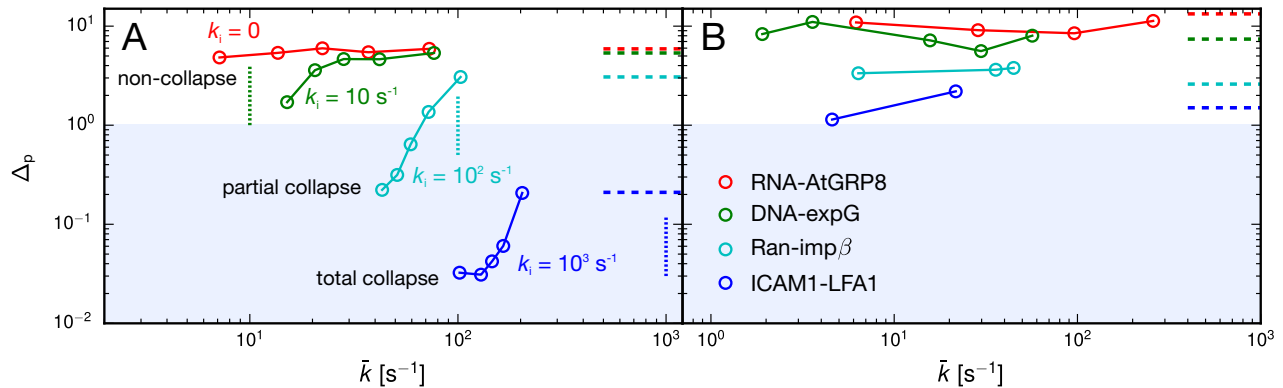


FIG. 3. Pair heterogeneity parameter Δ_p , calculated from a best-fit of $\Omega_r(f)$ curves for two consecutive values of loading rate (r_1, r_2) in a given data set. The horizontal axis coordinate is the smaller of the mean rupture rates for each pair, $\bar{k} = \min(\bar{k}(r_1), \bar{k}(r_2))$. For comparison, the Δ calculated from all loading rates in a data set is shown as a horizontal dashed line. The shaded region corresponds to $\Delta_p \leq 1$, where disorder is negligible. A) Results for the FBL model system of Fig. 2, with $\sigma = 0.05$ and $k_i = 0, 10, 10^2$, and 10^3 s^{-1} . From left to right, the Δ_p points for each k_i value correspond to loading rate pairs: $(r_1, r_2) = (200, 500), (500, 1000), (1000, 2000), (2000, 5000),$ and $(5000, 10000)$ pN/s. Vertical dotted lines mark the values of k_i in each case. Systems where $\Delta_p \geq 1$ across all measured time scales of $\bar{k}(r)$ must have slow conformational interconversion, $k_i < \bar{k}(r)$ or static disorder ($k_i = 0$), and thus correspond to the non-collapse (NC) regime. When some $\bar{k}(r)$ are larger than k_i and some are smaller, we are in the partial collapse (PC) regime, with smaller $\bar{k}(r)$ exhibiting $\Delta_p \ll 1$, and the larger ones $\Delta_p \geq 1$. When $k_i > \bar{k}(r)$ for the entire data set, all $\Delta_p \ll 1$, and we are in the total collapse (TC) regime. B) Results for four experimental systems (Fig. 6) that exhibit heterogeneity and have datasets with at least three loading rates. The Δ_p calculated from pairs of loading rates are consistent with the Δ calculated from the total data set, and all fall in the $\Delta_p \geq 1$ NC regime.

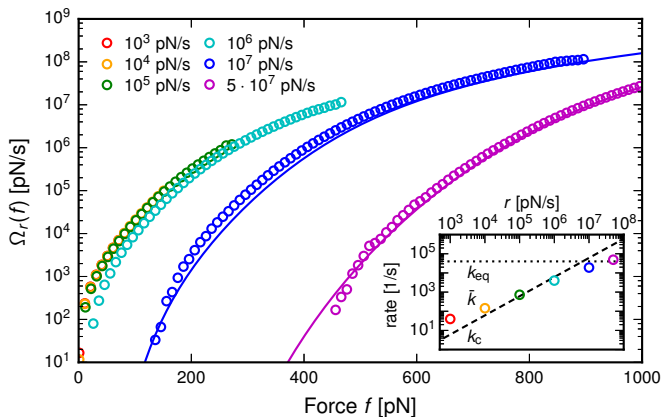


FIG. 4. Simulation results (circles) of $\Omega_r(f)$ for the FBL model system of Fig. 2, with no disorder ($\sigma = 0$) over a range of loading rates r extending into non-adiabatic regime. Each color is a different value of r . The solid curves for the two largest r are plots of the analytical expression in Eq. (9), derived for the model system in the $r \rightarrow \infty$ limit. The inset shows the mean rupture rate $\bar{k}(r)$ (circles) as a function of r compared to k_{eq} (dotted line) and $k_c(r)$ (dashed line).

indicate the presence of heterogeneity? To rule out the possibility of such a false positive, we simulated the FBL model system above, without any heterogeneity ($\sigma = 0$), over a much larger range of loading rates r , and plotted the results of $\Omega_r(f)$ in Fig. 4 on a logarithmic scale for $r = 10^3 - 5 \cdot 10^7$ pN/s. As shown in the figure inset,

for $r \lesssim 10^5$ pN/s, $\bar{k}(r)$ still falls between $k_c(r)$ and k_{eq} , so adiabaticity holds and the $\Omega_r(f)$ curves are nearly indistinguishable. However for $r \gtrsim 10^5$ pN/s the collapse begins to break down, and the $\Omega_r(f)$ curves grow increasingly distinct. Crucially, this non-adiabatic trend for a pure system is qualitatively different from what happens in the adiabatic heterogeneous case. In the former, the curves on a logarithmic plot grow more and more separated as r grows (Fig. 4), while in the latter situation the $\Omega_r(f)$ curves get closer together with increasing r (Fig. 2C). Thus a theory like Eq. (6)-(7), where convergence at large r is present ($\Omega_r(f) \rightarrow \kappa_1(f)$ as r increases), would not fit the non-adiabatic $\Omega_r(f)$ data, preventing a false positive. Indeed, for the model system used in our simulations, an expression for $\Sigma_r(f)$ in the non-adiabatic $r \rightarrow \infty$ limit can be analytically derived (details are in the SI) from an integral equation approach [26],

$$\Sigma_r(f) \rightarrow \frac{1}{2} \left(1 + \operatorname{erf} \left[\frac{\beta D x_0^\ddagger \omega_0^2 - r (e^{-\gamma} + \gamma - 1)}{D \sqrt{2\beta \omega_0^3 (1 - e^{-2\gamma})}} \right] \right), \quad (9)$$

where $\gamma \equiv \beta D f \omega_0 / r$. The corresponding analytical form for $\Omega_r(f) = -r \log \Sigma_r(f)$ is plotted in Fig. 4 as solid curves for the two largest values of r , comparing well with the simulated results. From Eq. (9) we can explicitly see that for a fixed f , $\Sigma_r(f) \rightarrow 1$ and $\Omega_r(f) \rightarrow 0$ as $r \rightarrow \infty$, so that the $\Omega_r(f)$ curves on a logarithmic plot like Fig. 4 are pushed increasingly downwards, the opposite trend of the theory in Eqs. (6)-(7). Thus in general, we should

be able to distinguish data sets corresponding to pure, non-adiabatic $\Omega_r(f)$ from heterogeneous, adiabatic ones, and false positives can be avoided.

Analysis of experimental data: As a demonstration of the wide applicability of our method, we have analyzed ten earlier datasets from biomolecular force ramp experiments, spanning a range of scales from strand separation in DNA oligomers up to the unbinding of large receptor-ligand complexes. Five of these systems (Fig. 5) showed TC of the $\Omega_r(f)$ curves, within experimental error bars, while the other five showed NC, and hence heterogeneity (Fig. 6). Let us consider each of these two groups in more detail.

Systems exhibiting TC: The five experimental studies exhibiting TC in Fig. 5 are: A) Schlierf & Rief [29], the unfolding of immunoglobulin-like domain 4 (ddFLN4) from *D. discoideum* F-actin cross-linker filamin. B) Koch & Wang [30], the unbinding of a complex between the restriction enzyme *Bso*BI and DNA. C) Neuert *et al.* [31], the unbinding of the steroid digoxigenin from an anti-digoxigenin antibody. D) Kim *et al.* [6], the unbinding of the von Willebrand factor A1 domain from the glycoprotein Ib α subunit (GPIb α). E) Manosas *et al.* [32], unzipping of an RNA hairpin. In the hairpin case, the collapse of the $\Omega_r(f)$ curves is consistent with collapse seen in other dynamical quantities extracted from the data at different loading rates, for example the rupture rate $k(f)$ or the effective barrier height at a given force [32, 33]. In all of the above experiments the data is originally gathered as time traces of the applied force. The rupture or unfolding event in each trace is identified as a large drop in the force when using AFM (or a large increase in the end-to-end distance using optical tweezers), a signature easily detected due to its high signal-to-noise ratio. The value of the force immediately before the drop is then recorded. From hundreds of such traces, the experimentalists construct the distribution of forces $p_v(f)$ or $p_r(f)$ at which the system unfolds/ruptures for a fixed pulling velocity v or loading rate r . In those cases (A,D) where data is reported in terms of v rather than r , mean values of the linker stiffness $\bar{\omega}_s$ are used to get corresponding loading rates $r = \bar{\omega}_s v$ (see the figure caption for values). The distribution $p_r(f)$ is related to $\Sigma_r(f)$ through $p_r(f) = -d\Sigma_r(f)/df$. By integrating $p_r(f)$ we obtain $\Sigma_r(f)$ and hence $\Omega_r(f)$. We can also calculate the mean rupture force $\bar{f}(r) = \int_0^\infty df f p_r(f)$ and thus the mean rupture rate $\bar{k}(r) = r/\bar{f}(r)$. The largest value of $\bar{k}(r)$ among all the r for a given experiment is shown in the bar chart of Fig. 5F. As mentioned above in discussing the TC scenario, the maximum observed value of $\bar{k}(r)$ provides a lower bound for both k_{eq} and k_i .

The local equilibration rate k_{eq} defines an intrinsic time scale whether or not the system is heterogeneous, but the slower interconversion rate k_i exists as a distinct time scale only when there is a heterogeneous ensemble of states with sufficiently large energy barriers between them. Observing collapse of $\Omega_r(f)$ over a range of r

does not absolutely rule out heterogeneity, but it does constrain the possible values of k_i . The two systems in Fig. 5 with the strongest constraints on k_i (the largest lower bounds) are A and C, where any k_i (or k_{eq}) must be $> \mathcal{O}(10^2 \text{ s}^{-1})$. This is not surprising, since A is a single, compact protein domain, and C is a tight antibody complex. For these systems, where specificity of the interactions stabilizing the functional state is of a prime importance, significant heterogeneity is unlikely, since it would require at least two conformational states involving substantially different sets of interactions. For the more general category of enzyme-substrate or receptor-ligand complexes (which encompasses systems B and D in Fig. 5 and all but one of the systems in Fig. 6), specificity may not always be the most important factor. Conformational heterogeneity among bound complexes could play crucial biological roles, as a part of enzymatic regulation or signaling.

System D of Fig. 5 presents an intriguing case, since force ramp experiments on the A1-GPIb α complex show evidence of two bound conformational states: a weaker bound state, from which the system is more likely to rupture at small forces ($\lesssim 10$ pN), and a more strongly bound state, predominating at larger forces [6]. The interconversion rates between the states could not be measured, but based on fitting the ramp data to a two-state model are estimated to be on the order of $\sim \mathcal{O}(1 \text{ s}^{-1})$. However the four experimental pulling velocities are so slow that the mean rupture rate at the highest velocity ($v = 40$ nm/s) is only 0.16 s^{-1} . Hence, if the two states do exist, they get averaged out over the timescale of rupture, leading to a set of $\Omega_r(f)$ curves that are collapsed. We can thus make a prediction for this particular system—assuming the two-state picture is reasonable and that both states are populated in the ensemble of complexes at the start of the force ramp. If the measurements were extended to velocities significantly above 40 nm/s, where rupture could occur on average before interconversion, the expanded data set should exhibit PC of the $\Omega_r(f)$ curves. As in the middle panel of Fig. 2D in the heterogeneous model system, the values of $\bar{k}(r)$ where PC occurs would roughly coincide with the interconversion rate k_i . This would be one way of directly estimating the scale of k_i from experiment.

Heterogeneous systems: In contrast to Fig. 5, the five experimental studies of Fig. 6 all show clear NC, and thus evidence of heterogeneity: A) Unbinding of the leukocyte function-associated antigen-1 (LFA1) integrin from its ligand, intercellular adhesion molecule-1 (ICAM1)[34]. B) Rupture of the GTPase protein Ran from the nuclear receptor importin β (imp β) [35]. For this dataset, Ran is loaded with a GTP analog (GppNHp), as well complexed with another binding partner, the protein RanBP1. C) Unzipping of a 10 basepair DNA duplex [36]. D) Raible *et al.* [22] (based on earlier experimental data from Ref. [37]), the unbinding of the regulatory protein expG from a promoter DNA fragment; E) Fuhrmann *et al.* [38], the unbinding of the protein ATGRP8 (in the mutant

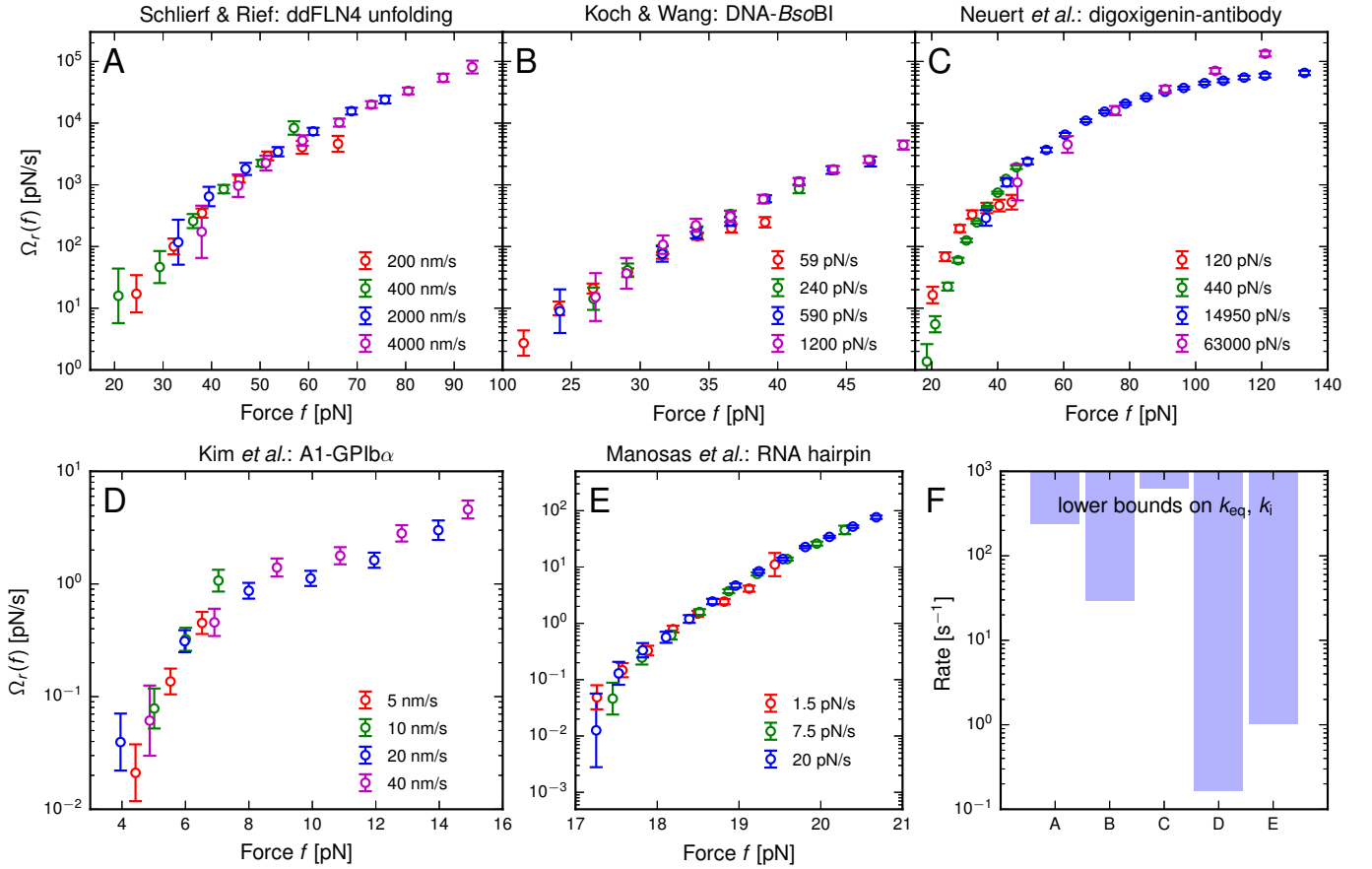


FIG. 5. Experimental $\Omega_r(f)$ data (circles) calculated from rupture force distributions in five studies: A) Ref. [29]; B) Ref. [30]; C) Ref. [31]; D) Ref. [6]. E) Ref. [32]. All these cases exhibit no apparent heterogeneity, with the $\Omega_r(f)$ curves for each system collapsing on one another. Colors denote different pulling velocities v or loading rates r , as reported in each study. For A and D, where v is reported, the linker stiffness values of $\bar{\omega}_s = 4.1$ (A) and 0.043 pN/nm (D) are used to get the corresponding loading rates $r = \bar{\omega}_s v$. F) For each of the experimental cases, the lower bounds on the possible values of k_{eq} and k_i , derived from the theoretical analysis.

ATGRP8-RQ form) from its RNA target.

In all these cases the theoretical fit to Eqs. (6)-(7) (solid curves) is excellent, allowing us to extract the fitting parameters listed in each panel of Fig. 6. The values of k_0 , the effective zero-force off-rate, are in the range $\sim \mathcal{O}(0.01 - 0.1 \text{ s})$, while the effective transition state distance $b \sim \mathcal{O}(0.1 - 1 \text{ nm})$. Both of these scales are physically sensible for protein or nucleic acid systems. The panels in Fig. 6 are ordered by increasing Δ , which varies from 1.5 to 13.3. To verify the robustness of these Δ values, we also calculated the pair parameters Δ_p for every data set that had at least three different loading rates. These are shown in Fig. 3B, with the corresponding Δ for the full data indicated as horizontal dashed lines. As is expected for the NC regime, the Δ_p do not vary significantly with rupture rate, and are consistent with Δ in each case. The three largest values of Δ (Fig. 6C-E) correspond to bonds composed of nucleic acid base-pairing or protein/nucleic acid interactions. This significant heterogeneity may reflect the tendency for free energy landscapes involving nucleic acids to be more intrinsically

rugged. However it is not necessarily the case that all nucleic acid systems are heterogeneous (the *BsoBI*-DNA complex of Fig. 5B and the RNA hairpin of Fig. 5E are counter-examples).

All the data in Fig. 6 was collected using AFM pulling experiments, in contrast to Fig. 5, where panels B, D, and E were optical trap results (the rest being AFM). It is thus worthwhile to wonder whether aspects of the AFM experimental setup could affect the heterogeneity analysis. In SI Sec. 5 we have analyzed possible errors from several sources: the finite force resolution of AFM cantilever, the non-negligible hydrodynamic drag on the cantilever at large pulling speeds ($\dot{\gamma} 1 \mu\text{m/s}$) [39–41], uncertainties arising from finite sampling of the rupture force distributions, and the apparatus response time. Based on this error analysis, we conclude that the estimation of the heterogeneity parameter Δ from the experimental data is reliable in all the systems of Fig. 6. The observed heterogeneity must therefore be an intrinsic aspect to the biomolecules, rather than an artifact of the AFM experiment.

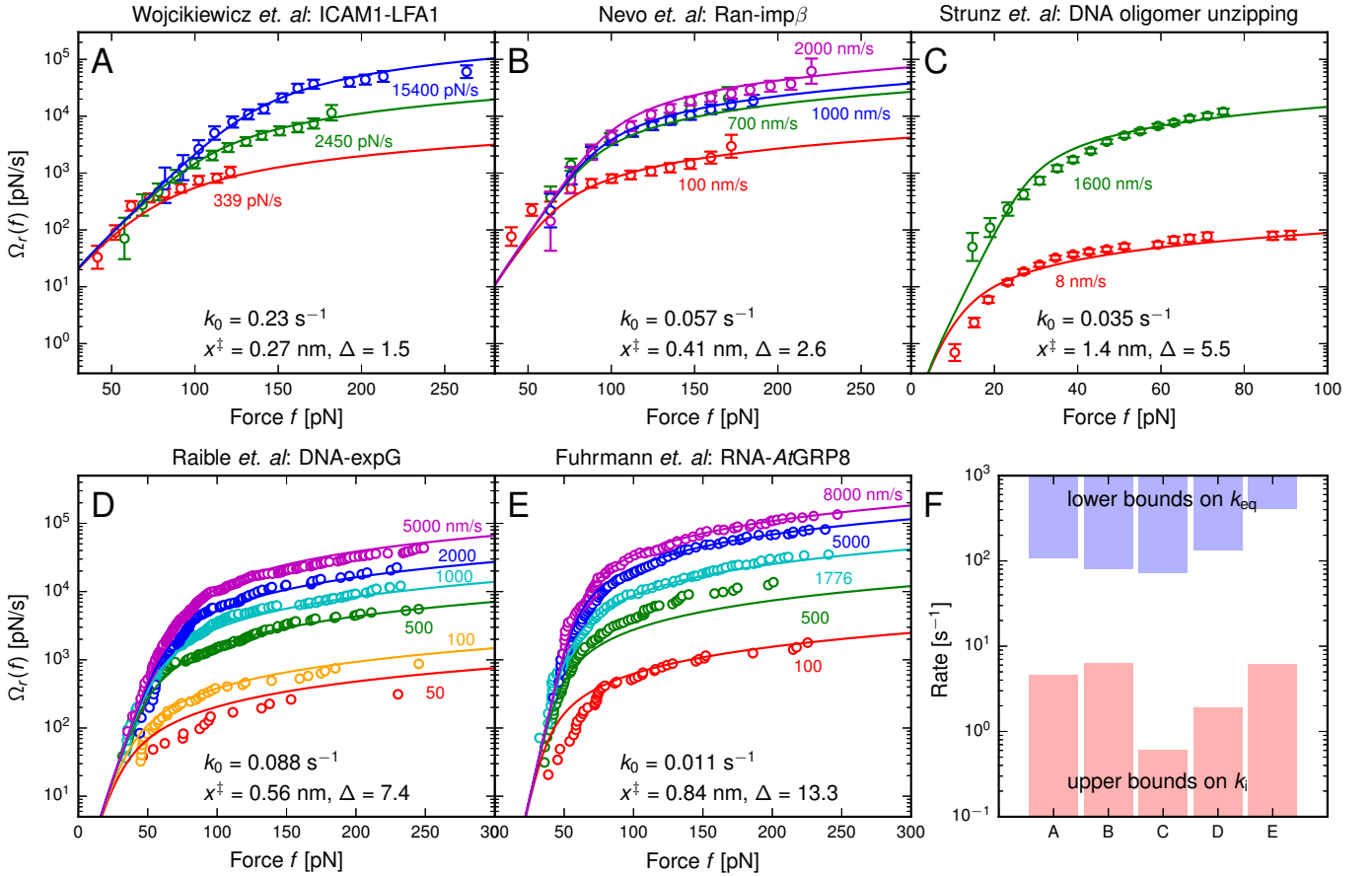


FIG. 6. Experimental $\Omega_r(f)$ data (circles) calculated from rupture force distributions in five studies: A) Ref. [34]; B) Ref. [35]; C) Ref. [36]; D) Ref. [22]; E) Ref. [38]. In contrast to Fig. 5, these systems exhibit heterogeneity, with distinct $\Omega_r(f)$ curves. Colors denote different pulling velocities v or loading rates r , as reported in each study. For B-E, where v is reported, the linker stiffness values of $\bar{\omega}_s = 5.0$ (B), 2.0 (C), 3.0 (D), and 6.0 pN/nm (E) are used to get the corresponding loading rates $r = \bar{\omega}_s v$. Solid curves show the theoretical best-fit to Eqs. (6)-(7), with the fitted parameters k_0 , x^\ddagger , and Δ listed in each panel. F) For each of the experimental cases, the lower bounds on the possible values of k_{eq} (blue bars) and the upper bounds on k_i (pink bars), derived from the theoretical analysis.

The fidelity of the theoretical fits to the data in Fig. 6 (with no signs of PC) means all the experiments were in the heterogeneous, adiabatic regime. Thus the range of observed $k(r)$ allows us to place upper bounds on k_i and lower bounds on k_{eq} , which are plotted in the bar chart of Fig. 6F. There is a clear separation of time scales, with all the upper bounds on $k_i \lesssim 10 \text{ s}^{-1}$, and the lower bounds on $k_{\text{eq}} \gtrsim 10^2 \text{ s}^{-1}$. The slow interconversion rates k_i in these systems are remarkable, particularly the DNA oligomer in Fig. 6C, which is a tiny system only 10 base-pairs long. The rupture force distributions for the DNA unzipping were earlier fit to a specific model of dynamic disorder in Ref. [23], where force-dependent rates of conformational fluctuations were extracted. The range of these estimated rates ($2.8 \times 10^{-5} - 4.8 \times 10^{-1} \text{ s}^{-1}$) are consistent with the upper bound derived from the current analysis, $k_i < 0.6 \text{ s}^{-1}$. However, we must keep in mind that—unless PC is observed, pinpointing the scale of k_i —our analysis cannot distinguish between a heterogeneous system characterized by dynamic disorder with

slow k_i and one with quenched disorder ($k_i = 0$) caused by covalent chemical differences among the experimental samples.

The Ran-imp β system in Fig. 6B provides an interesting counterpart to the A1-GPIb α complex discussed earlier. As in that example, the system is believed to exhibit two bound conformations with different adhesion strengths [35, 42]. This is also supported by evidence of conformational variability in the crystal structure of a truncated imp β bound to Ran-GppNHP, where two versions of the molecular complex were observed, characterized by substantially different sets of interactions [43]. The bound conformations are expected to dynamically interconvert, but the timescale has not been measured. Our analysis of the existing data provides an upper bound on the rate, $k_i < 6.4 \text{ s}^{-1}$. We predict that further experiments could fix the rate more precisely: for example, by going to pulling velocities slower than $v = 100 \text{ nm/s}$ (the slowest v in the current dataset), we may be able to observe PC, like in the middle panel

in Fig. 2D, establishing the scale of k_i . This is opposite of the prescription we gave above for the A1-GPIb α complex, where the existing experiments have been too slow rather than too fast. Our theory thus provides a guide for experimentalists to fine-tune their parameters to extract the most information possible from the system under study.

We envision that our approach will become one part of a larger, comprehensive experimental toolbox for investigating heterogeneity in biomolecules: it can test for and quantify heterogeneity based on the rupture force distributions, but these distributions do not contain all the information we would like to know about a system. A large Δ parameter indicates that there are multiple states in the intact/folded part of the free energy landscape, and that these states must interconvert on timescales slower than the mean rupture time. To extract additional details, like the precise number of functional states, requires using other experimental/analytical techniques, like single-molecule FRET. One recent example where this was demonstrated was the k -means clustering algorithm applied by Hyeon *et al.* [16] to estimate the number of interconverting states from single-molecule FRET trajectories of a simple nucleic acid construct, the Holliday junction. In principle, this approach could be extended to folding trajectories obtained in constant force experiments, which in conjunction with the distribution of rupture forces could be used to extract the number of distinct functional states.

CONCLUSIONS

Our work introduces a generic method for characterizing heterogeneity in biomolecules using rupture force distributions from force spectroscopy experiments. The central result is a single non-dimensional parameter $\Delta \geq 0$. A system with no measurable heterogeneity on the timescale of the pulling experiment has $\Delta = 0$. When

$\Delta > 0$, its magnitude characterizes the degree of the disorder. Both in the presence and absence of heterogeneity, the method yields bounds on the local equilibration rate k_{eq} within a system state, and (if heterogeneity is present) the rate of interconversion k_i between states. The practical value of our approach is demonstrated by analyzing nine previous experiments, allowing us to classify a broad range of biomolecular systems. The five cases where heterogeneity was observed are all the more striking given the persistence of their conformational states, with upper bounds on $k_i \lesssim 10 \text{ s}^{-1}$.

Our theory leads to a proposal for future experimental studies: searching for a range of pulling speeds where the data exhibits the property of partial collapse, allowing for a more accurate determination of k_i . This PC scenario did not occur among the data sets we considered, though in two cases (the protein complexes A1-GPIb α and Ran-imp β) we predict that extending the range of pulling velocities would very likely result in PC. The global energy landscapes of multi-domain protein and nucleic acid systems are essential guides to their biological function, but are quite difficult to map out in the laboratory. This is particularly true for systems where the ruggedness of the landscape creates a host of long-lived, functional states. The theory described here suggests new ways in which single molecule pulling experiments can be used to obtain information about internal dynamics of systems with functionally heterogeneous states. Our technique should shed new light on both the static and dynamic aspects of such landscapes, the first step towards a comprehensive structural understanding of these biomolecular shape-shifters.

ACKNOWLEDGMENTS

This work was initiated when M.H. and D.T. were visiting scholars in KIAS in 2013.

-
- [1] Altschuler SJ, Wu LF (2010) Cellular heterogeneity: do differences make a difference? *Cell* 141:559–563.
 - [2] Lu HP, Xun L, Xie XS (1998) Single-molecule enzymatic dynamics. *Science* 282:1877–1882.
 - [3] van Oijen AM, et al. (2003) Single-molecule kinetics of λ exonuclease reveal base dependence and dynamic disorder. *Science* 301:1235–1238.
 - [4] English BP, et al. (2005) Ever-fluctuating single enzyme molecules: Michaelis-menten equation revisited. *Nat. Chem. Biol.* 2:87–94.
 - [5] Solomatin SV, Greenfeld M, Chu S, Herschlag D (2010) Multiple native states reveal persistent ruggedness of an rna folding landscape. *Nature* 463:681–684.
 - [6] Kim J, Zhang CZ, Zhang X, Springer TA (2010) A mechanically stabilized receptor-ligand flex-bond important in the vasculature. *Nature* 466:992–995.
 - [7] Buckley CD, et al. (2014) The minimal cadherin-catenin complex binds to actin filaments under force. *Science* 346:1254211.
 - [8] Austin RH, Beeson KW, Eisenstein L, Frauenfelder H, Gunsalus IC (1975) Dynamics of ligand binding to myoglobin. *Biochem.* 14:5355–5373.
 - [9] Frieden C (1979) Slow transitions and hysteretic behavior in enzymes. *Annu. Rev. Biochem.* 48:471–489.
 - [10] Schmid FX, Blaschek H (1981) A native-like intermediate on the ribonuclease a folding pathway. *Eur. J. Biochem.* 114:111–117.
 - [11] Agmon N, Hopfield JJ (1983) Transient kinetics of chemical reactions with bounded diffusion perpendicular to the reaction coordinate: intramolecular processes with slow conformational changes. *J. Chem. Phys.* 78:6947–6959.
 - [12] Frauenfelder H, Parak F, Young RD (1988) Conforma-

- tional substates in proteins. *Annu. Rev. Biophys. Biochem. Chem.* 17:451–479.
- [13] Honeycutt J, Thirumalai D (1990) Metastability of the folded states of globular proteins. *Proc. Natl. Acad. Sci.* 87:3526–3529.
- [14] Zwanzig R (1990) Rate processes with dynamical disorder. *Acc. Chem. Res.* 23:148–152.
- [15] Zwanzig R (1992) Dynamical disorder: passage through a fluctuating bottleneck. *J. Chem. Phys.* 97:3587–3589.
- [16] Hyeon C, Lee J, Yoon J, Hohng S, Thirumalai D (2012) Hidden complexity in the isomerization dynamics of holiday junctions. *Nature Chem.* 4:907.
- [17] Kowerko D, et al. (2015) Cation-induced kinetic heterogeneity of the intron-exon recognition in single group II introns. *Proc. Natl. Acad. Sci.* 112:3403–3408.
- [18] Liu B, Baskin RJ, Kowalczykowski SC (2013) Dna unwinding heterogeneity by RecBCD results from static molecules able to equilibrate. *Nature* 500:482.
- [19] Pressé S, Lee J, Dill KA (2013) Extracting conformational memory from single-molecule kinetic data. *J. Phys. Chem. B* 117:495–502.
- [20] Raible M, Evstigneev M, Reimann P, Bartels FW, Ros R (2004) Theoretical analysis of dynamic force spectroscopy experiments on ligand–receptor complexes. *J. Biotech.* 112:13–23.
- [21] Raible M, Reimann P (2006) Single-molecule force spectroscopy: Heterogeneity of chemical bonds. *EPL* 73:628.
- [22] Raible M, et al. (2006) Theoretical analysis of single-molecule force spectroscopy experiments: heterogeneity of chemical bonds. *Biophys. J.* 90:3851–3864.
- [23] Hyeon C, Hinczewski M, Thirumalai D (2014) Evidence of disorder in biological molecules from single molecule pulling experiments. *Phys. Rev. Lett.* 112:138101.
- [24] Thirumalai D, Hyeon C (2005) RNA and Protein folding: Common Themes and Variations. *Biochemistry* 44:4957–4970.
- [25] Evans E, Ritchie K (1997) Dynamic strength of molecular adhesion bonds. *Biophys. J.* 72:1541–1555.
- [26] Hu Z, Cheng L, Berne B (2010) First passage time distribution in stochastic processes with moving and static absorbing boundaries with application to biological rupture experiments. *J. Chem. Phys.* 133:034105.
- [27] Bullerjahn JT, Sturm S, Kroy K (2014) Theory of rapid force spectroscopy. *Nature Commun.* 5:4463.
- [28] Dudko OK, Hummer G, Szabo A (2006) Intrinsic rates and activation free energies from single-molecule pulling experiments. *Phys. Rev. Lett.* 96:108101.
- [29] Schlierf M, Rief M (2006) Single-molecule unfolding force distributions reveal a funnel-shaped energy landscape. *Biophys. J.* 90:L33–L35.
- [30] Koch SJ, Wang MD (2003) Dynamic force spectroscopy of protein-DNA interactions by unzipping DNA. *Phys. Rev. Lett.* 91:028103.
- [31] Neuert G, Albrecht C, Pamir E, Gaub H (2006) Dynamic force spectroscopy of the digoxigenin–antibody complex. *FEBS Lett.* 580:505–509.
- [32] Manosas M, Collin D, Ritort F (2006) Force-dependent fragility in RNA hairpins. *Phys. Rev. Lett.* 96:218301.
- [33] Bizarro CV, Alemany A, Ritort F (2012) Non-specific binding of Na^+ and Mg^{2+} to RNA determined by force spectroscopy methods. *Nucl. Acid* 40:6922–6935.
- [34] Wojcikiewicz EP, Abdulreda MH, Zhang X, Moy VT (2006) Force spectroscopy of LFA-1 and its ligands, ICAM-1 and ICAM-2. *Biomacromolecules* 7:3188–3195.
- [35] Nevo R, Brumfeld V, Elbaum M, Hinterdorfer P, Reich Z (2004) Direct discrimination between models of protein activation by single-molecule force measurements. *Biophys. J.* 87:2630–2634.
- [36] Strunz T, Oroszlan K, Schäfer R, Güntherodt HJ (1999) Dynamic force spectroscopy of single DNA molecules. *Proc. Natl. Acad. Sci.* 96:11277–11282.
- [37] Bartels FW, Baumgarth B, Anselmetti D, Ros R, Becker A (2003) Specific binding of the regulatory protein ExpG to promoter regions of the galactoglucan biosynthesis gene cluster of *Sinorhizobium meliloti*—a combined molecular biology and force spectroscopy investigation. *J. Struct. Biol.* 143:145–152.
- [38] Fuhrmann A, Schoening JC, Anselmetti D, Staiger D, Ros R (2009) Quantitative analysis of single-molecule rna-protein interaction. *Biophys. J.* 96:5030–5039.
- [39] Alcaraz J, et al. (2002) Correction of microrheological measurements of soft samples with atomic force microscopy for the hydrodynamic drag on the cantilever. *Langmuir* 18:716–721.
- [40] Janovjak H, Struckmeier J, Müller DJ (2005) Hydrodynamic effects in fast AFM single-molecule force measurements. *Eur. Biophys. J.* 34:91–96.
- [41] Liu R, Roman M, Yang G (2010) Correction of the viscous drag induced errors in macromolecular manipulation experiments using atomic force microscope. *Rev. Sci. Instr.* 81:063703.
- [42] Nevo R, et al. (2003) A molecular switch between alternative conformational states in the complex of ran and importin β 1. *Nature Struct. Mol. Biol.* 10:553–557.
- [43] Vetter IR, Nowak C, Nishimoto T, Kuhlmann J, Wittinghofer A (1999) Structure of a ran-binding domain complexed with ran bound to a GTP analogue: implications for nuclear transport. *Nature* 398:39–46.
- [44] Ermak DL, McCammon JA (1978) Brownian dynamics with hydrodynamic interactions. *J. Chem. Phys.* 69:1352–1360.
- [45] Kampen NGv (2007) *Stochastic processes in physics and chemistry* (Elsevier, Amsterdam).
- [46] Neuman KC, Nagy A (2008) Single-molecule force spectroscopy: optical tweezers, magnetic tweezers and atomic force microscopy. *Nat. Methods* 5:491–505.
- [47] Viani MB, et al. (1999) Small cantilevers for force spectroscopy of single molecules. *J. Appl. Phys.* 86:2258–2262.

Supplementary information for:

“Directly measuring single molecule heterogeneity using force spectroscopy”

Michael Hinczewski, Changbong Hyeon, D. Thirumalai

1. TESTING THE ASSUMPTIONS OF THE $\Omega_r(f)$ MODEL WITH RESPECT TO POSSIBLE GENERALIZATIONS

The general form for $\Omega_r(f)$ introduced in Eq. (6) of the main text,

$$\Omega_r(f) \approx \frac{r}{\Delta(f)} \log \left(1 + \frac{\kappa_1(f)\Delta(f)}{r} \right), \quad (\text{S1})$$

depends on the functions $\Delta(f)$ and $\kappa_1(f)$. For the analysis of the experimental data, we chose a minimal model for these two functions, shown in Eq. (7):

$$\Delta(f) = \Delta, \quad \kappa_1(f) = \frac{k_0}{\beta x^\ddagger} \left(e^{\beta f x^\ddagger} - 1 \right). \quad (\text{S2})$$

This assumes $\Delta(f)$ is constant across the force range of the experiment, and $\kappa_1(f)$ takes the same mathematical form as in the case of a pure Bell model, $\kappa_1(f) = \int_0^f df' k(f')$, where $k(f) = k_0 e^{\beta f x^\ddagger}$. The result is a three parameter model (depending on Δ , k_0 , x^\ddagger) that is able to simultaneously fit $\Omega_r(f)$ data for loading rates across two to three orders of magnitude for a large number of unrelated biological systems.

However, it is worthwhile to ask if the general conclusions that we draw from the experimental fitting would change substantially if the above assumptions were relaxed, and we used more complicated forms for $\Delta(f)$ and $\kappa_1(f)$. Here we will examine two generalizations of the minimal model (in each adding another fitting parameter) and verify that our characterization of heterogeneity in the experimental systems is indeed robust.

i) *Dudko-Hummer-Szabo model for $k(f)$* : The most widely used generalization of the Bell model was introduced by Dudko, Hummer, and Szabo (DHS) [28]. In this approach, the escape rate $k(f)$ is calculated from Kramers theory for particular choices of the underlying 1D free energy profile, leading to

$$k_{\text{DHS}}(f) = k_0 \left(1 - \frac{\nu f x^\ddagger}{G^\ddagger} \right)^{\frac{1}{\nu} - 1} e^{\beta G^\ddagger [1 - (1 - \nu f x^\ddagger / G^\ddagger)^{1/\nu}]}, \quad (\text{S3})$$

which introduces two extra parameters: G^\ddagger , the height of the free energy barrier at zero force, and ν , characterizing the shape of the 1D free energy profile, in addition to x^\ddagger (the transition state distance) and k_0 (the rate at zero force). The constant ν is usually chosen to be either 2/3 or 1/2, corresponding to linear-cubic or cusp-like free energy profiles respectively. We use $\nu = 2/3$ in the analysis below, though the results were similar for $\nu = 1/2$. With the escape rate $k_{\text{DHS}}(f)$, the generalized form for $\kappa_1(f) = \int_0^f df' k_{\text{DHS}}(f')$ becomes:

$$\kappa_1(f) = \frac{k_0}{\beta x^\ddagger} \left(e^{\beta G^\ddagger [1 - (1 - \nu f x^\ddagger / G^\ddagger)^{1/\nu}]} - 1 \right). \quad (\text{S4})$$

Substituting this for $\kappa_1(f)$, with ν fixed at 2/3, in Eq. (S2) we have a four parameter model for $\Omega_r(f)$, depending on Δ , k_0 , x^\ddagger , and G^\ddagger .

In the limit of $G^\ddagger \rightarrow \infty$ the DHS model reduces to the original Bell form, and hence the results for $\Omega_r(f)$ are the same as in the minimal model. For $G^\ddagger < \infty$ the DHS form introduces small corrections, shown in Fig. S1, particularly at larger forces where the increase in $\Omega_r(f)$ is not as rapid as in the Bell version. Note that in fitting to experimental data, the parameter G^\ddagger cannot be made smaller than $f_{\text{max}} \nu x^\ddagger$, where f_{max} is the largest force value that appears in the data set. The DHS model is not mathematically defined for G^\ddagger below that cutoff. Fig. S2 shows three sets of experimental results for $\Omega_r(f)$ from Fig. 6 of the main text, comparing the minimal model fits (solid curves) to the best-fit using the more complex DHS model (dashed curves). These three systems yielded G^\ddagger values in the range 16 – 53 $k_B T$. (The other two experimental systems from Fig. 6 did not exhibit any improved fitting using the DHS model, since the best-fit G^\ddagger was large enough that the results were numerically indistinguishable from the minimal Bell model.) The DHS fits for $\Omega_r(f)$ in Fig. S2 are very close to the minimal model fits, and the extracted Δ values from the two approaches differ by only 5 – 20%, a discrepancy comparable to the uncertainty in Δ due to finite

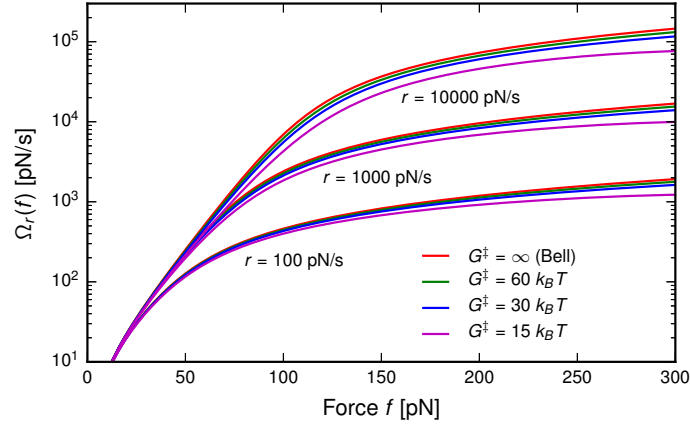


FIG. S1. $\Omega_r(f)$ curves of the FBL model for $r = 100, 1000$ and 10000 pN/s using the DHS form for $\kappa_1(f)$ [Eq. (S4)]. The parameters are $\Delta = 5$, $k_0 = 0.1 \text{ s}^{-1}$, $x^\ddagger = 0.3 \text{ nm}$, and various values for G^\ddagger , ranging from ∞ (red curves, corresponding to the Bell limit) down to $15 k_B T$ (purple curves).

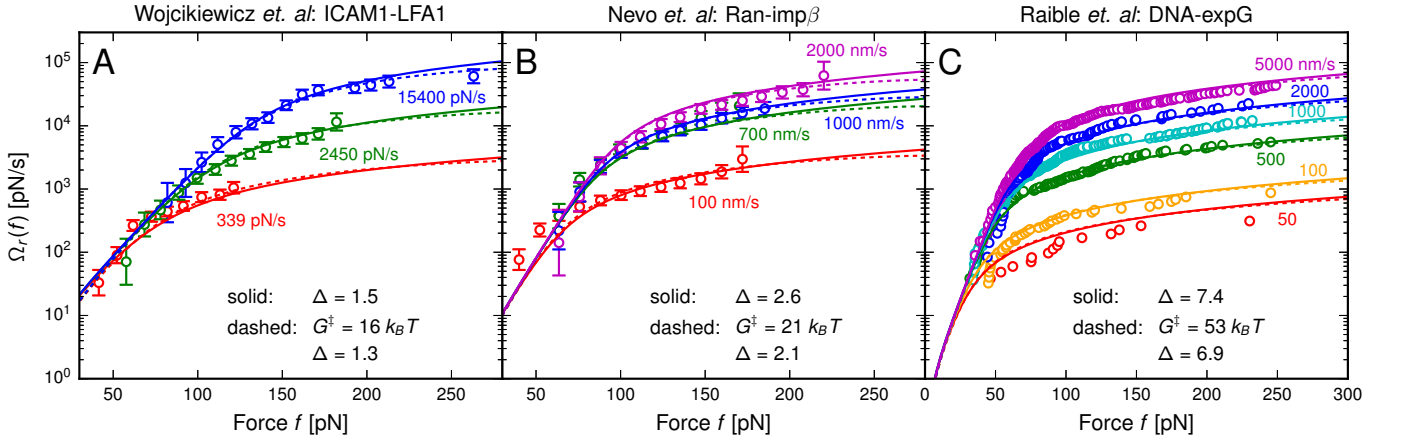


FIG. S2. Experimental $\Omega_r(f)$ data (circles) calculated from rupture force distributions in three studies: A) Ref. [34]; B) Ref. [35]; C) Ref. [22]. Colors denote different pulling velocities v or loading rates r , as reported in each study. For B-C, where v is reported, the linker stiffness values of $\bar{k}_s = 5.0$ (B) and 3.0 (C) are used to get the corresponding loading rates $r = \bar{k}_s v$. Solid curves show the theoretical best-fit for the minimal three-parameter model (Eqs. (S1)-(S2)) with the extracted value of Δ indicated in the panel. The dashed curves are the best-fits from the four-parameter DHS model ($\kappa_1(f)$ replaced by Eq. (S4)) with the values for G^\ddagger and Δ listed at the bottom of the panel.

sampling of the rupture force distribution (see SI Sec. 5.ii below). Thus, at least for the data sets we have looked at, the Bell approximation is justifiable, and does not affect our heterogeneity analysis in terms of Δ in a significant way.

ii) *Linearly varying $\Delta(f)$* : The second generalization of the minimal model which we consider is relaxing the assumption that $\Delta(f)$ is constant across the measured force range. At lowest order we can allow $\Delta(f)$ to be a linear function of f , $\Delta(f) = \Delta_0 + f/f_0$, where Δ_0 and f_0 are constants. This leads to a four parameter model for $\Omega_r(f)$, depending on Δ_0 , f_0 , k_0 , and x^\ddagger . Fig. S3 shows $\Omega_r(f)$ for all five experimental systems from Fig. 6 of the main text, and compares the best-fit results for the constant versus linear $\Delta(f)$ models. The shapes of the $\Omega_r(f)$ curves from the two approaches are very similar. To compare the predicted heterogeneity from the two models, we calculated the average $\bar{\Delta}$ of the linear $\Delta(f)$ best-fit function across the range of experimentally measured forces in each case. The difference between $\bar{\Delta}$ and the best-fit value for Δ in the minimal model was less than 20% in all the systems. This confirms that assuming constant $\Delta(f)$ in the minimal model gives a reasonable estimate of the average of $\Delta(f)$ over the experimental force range.

Thus, both generalizations of the minimal model lead to quantitatively similar results for heterogeneity in the experimental data. Following the Occam's razor principle, we thus have confined our analysis in the main text to the three parameter model for $\Omega_r(f)$, which has the added benefit of a simpler interpretation. However, it is conceivable

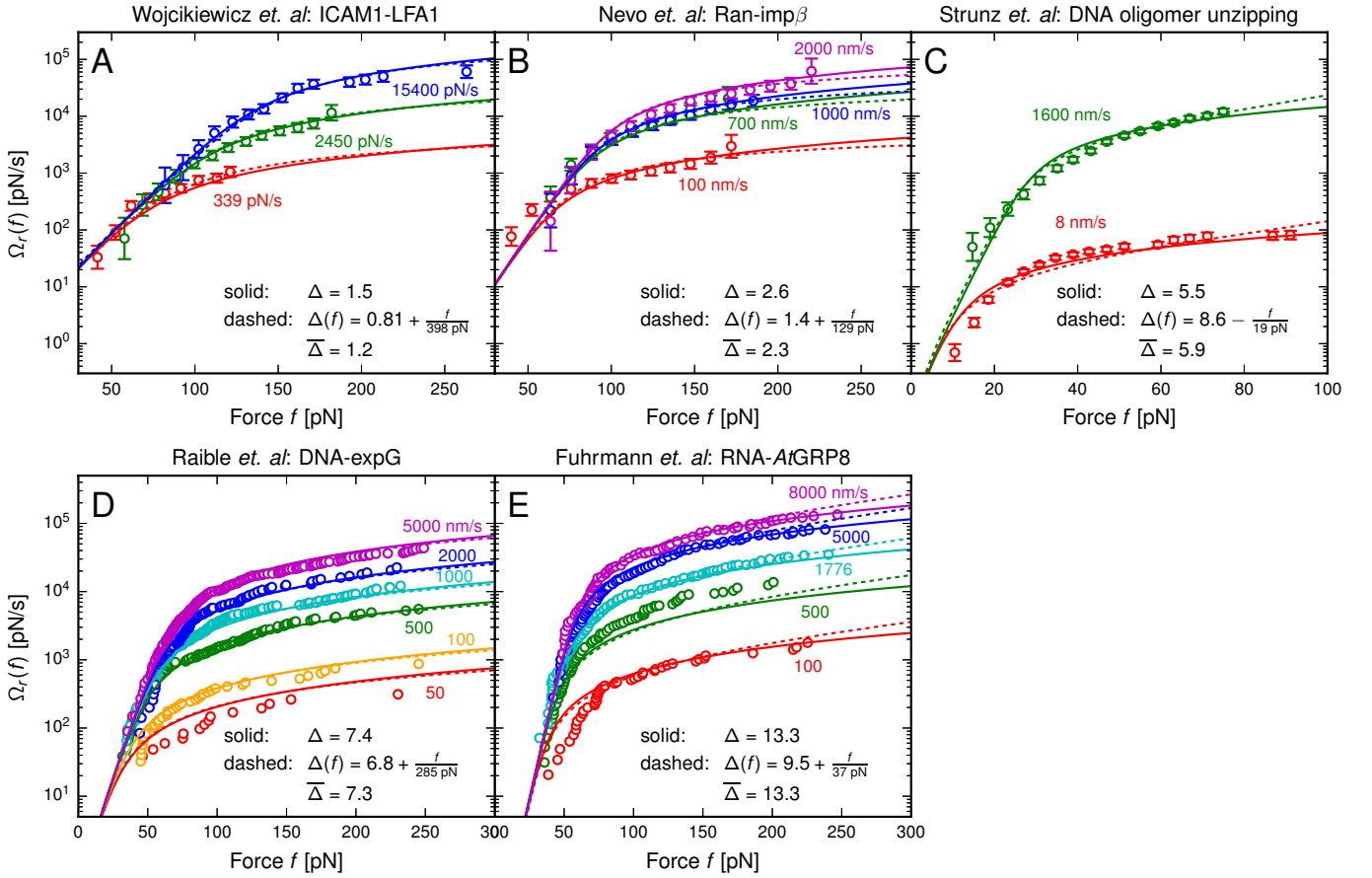


FIG. S3. Experimental $\Omega_r(f)$ data (circles) calculated from rupture force distributions in five studies: A) Ref. [34]; B) Ref. [35]; C) Ref. [36]; D) Ref. [22]; E) Ref. [38]. Colors denote different pulling velocities v or loading rates r , as reported in each study. For B-E, where v is reported, the linker stiffness values of $\bar{k}_s = 5.0$ (B), 2.0 (C), 3.0 (D), and 6.0 pN/nm (E) are used to get the corresponding loading rates $r = \bar{k}_s v$. Solid curves show the theoretical best-fit for the minimal three-parameter model (Eqs. (S1)-(S2)) with the extracted value of Δ indicated in the panel. The dashed curves are the best-fits from the four-parameter model where $\Delta(f)$ varies linearly with f . The fit results for $\Delta(f)$ are shown at the bottom of the panel, together with the average value $\bar{\Delta}$ of $\Delta(f)$ across the experimental force range.

that future data sets might require one or both of these extensions for reasonable fitting, due to specific details of the biological system. The generality of Eq. (S1) easily accommodates these extensions and more, allowing us to incorporate complex parametrizations of $\Delta(f)$ and $\kappa_1(f)$ if necessary.

2. HETEROGENEOUS MODEL SIMULATION DETAILS

The heterogeneous model in the main text describes diffusion along a reaction coordinate x characterized by a diffusivity D and a free energy at zero force $U(x) = (1/2)\omega_0 x^2$. If the system undergoes pulling at a constant force ramp rate r , the potential becomes time-dependent, $U(x, t) = (1/2)\omega_0 x^2 - rtx$. Each simulation trajectory is generated using Brownian dynamics [44] on this potential, with parameters $r = 200 - 10000$ pN/s, $D = 100$ nm²/s, $\omega_0 = 400$ $k_B T$ /nm², $x_0^\ddagger = 0.2$ nm. The simulation time step is $\Delta t = 0.1$ μ s. The system is initialized at $x = 0$ and $x^\ddagger = x_0^\ddagger$, and run until the rupture occurs, $x \geq x^\ddagger$. At every time step, along with the Brownian dynamics update of x , we also include the possibility of conformational interconversion as a Poisson process: a random number η between 0 and 1 is chosen; if $\eta > \exp(-k_i \Delta t)$, a new value of x^\ddagger is drawn from the Gaussian distribution $P(x^\ddagger) = \exp(-(x^\ddagger - x_0^\ddagger)^2 / 2\sigma^2) / \sqrt{2\pi\sigma^2}$. The ranges of distribution widths and interconversion rates are $\sigma = 0 - 0.05$ nm, $k_i = 0 - 10^4$ s⁻¹. The rupture event at the end of a trajectory occurs at a particular time t , corresponding to a force $f = rt$. By collecting about 3×10^4 trajectories for each value of r , we get a rupture force distribution $p_r(f)$. The survival probability $\Sigma_r(f)$ is the cumulative distribution $\Sigma_r(f) = 1 - \int_0^f df' p(f')$, from which

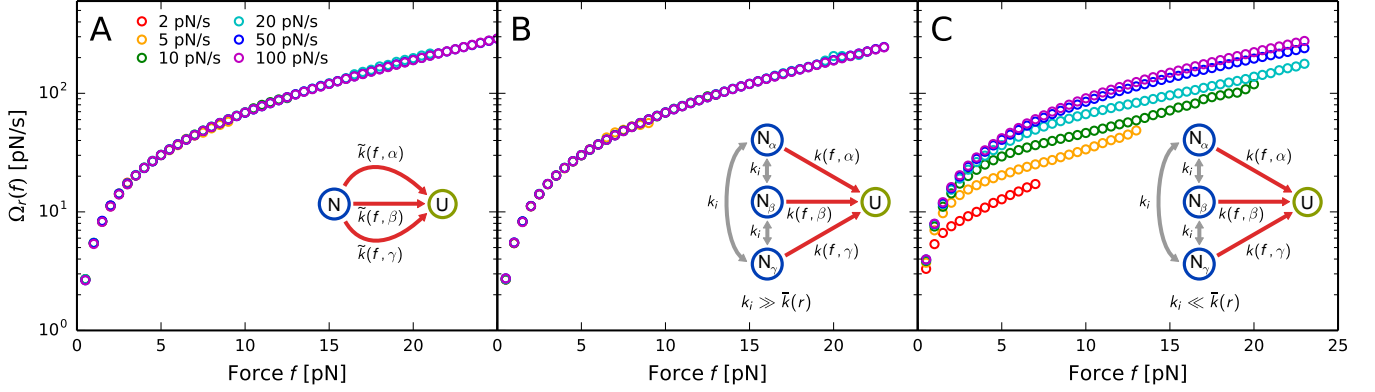


FIG. S4. A) A system with three different rupture pathways between the native (N) and unbound (U) states. The transition rates for each pathway at force f are given by: $\tilde{k}(f, \alpha) = 10 \text{ s}^{-1} e^{\beta f(0.1 \text{ nm})}$, $\tilde{k}(f, \beta) = 1 \text{ s}^{-1} e^{\beta f(0.5 \text{ nm})}$, $\tilde{k}(f, \gamma) = 5 \text{ s}^{-1} e^{\beta f(0.3 \text{ nm})}$. Assuming a force ramp $f(t) = rt$, the corresponding master equation for the time evolution of the system is solved numerically, and the results for $\Omega_r(f)$ are plotted for six different ramp rates r between 2 and 100 pN/s. B) Analogous to panel A, but for a system with multiple native states, interconverting at rate k_i . The rupture rate functions are a factor of 3 times larger than their counterparts in A, for example $k(f, \alpha) = 3\tilde{k}(f, \alpha)$. The value $k_i = 1000 \text{ s}^{-1}$ is large enough that $k_i \gg \bar{k}(r)$, the mean rate of rupture at each r . C) Same as in panel B, but with $k_i = 0.1 \text{ s}^{-1} \ll \bar{k}(r)$.

we can then calculate $\Omega_r(f) = -r \log \Sigma_r(f)$.

3. HETEROGENEITY IN RUPTURE PATHWAYS VERSUS HETEROGENEITY IN FUNCTIONAL STATES

The heterogeneity discussed in the main text refers to the presence of multiple, distinct functional states N_α , each characterized by a certain rupture rate at constant force, $k(f, \alpha)$. But biomolecules can also exhibit another kind of heterogeneity, where a native basin of attraction has multiple dynamic pathways by which the system can unfold or rupture to reach state U. In fact, the two kinds of heterogeneity can in principle exist in the same system. Fig. S4A depicts a simple model that is heterogeneous in the second sense (though not the first): a single native state N has three rupture pathways, labeled α , β , and γ , with corresponding rate functions $\tilde{k}(f, \alpha)$, $\tilde{k}(f, \beta)$, and $\tilde{k}(f, \gamma)$. At a certain force f , this is equivalent to a total rate of transitioning from N to U given by $k(f) = \tilde{k}(f, \alpha) + \tilde{k}(f, \beta) + \tilde{k}(f, \gamma)$. Assuming adiabaticity under a force ramp $f(t)$, the survival probability $\Sigma_r(t)$ obeys the kinetic equation $d\Sigma_r(t)/dt = -k(f(t))\Sigma_r(t)$, and the same arguments apply as for the pure system in the main text, leading to collapse of the $\Omega_r(f)$ curves. We verify this numerically for the model system, solving the associated master equation. We show the $\Omega_r(f)$ results in Fig. S4A for particular choices of \tilde{k} described in the caption.

It is instructive to compare this multiple-pathway, single-native-state system to the functionally heterogeneous system shown in Fig. S4B. Here there are three native states N_α , N_β , and N_γ , with corresponding rupture rate functions $k(f, \alpha)$, $k(f, \beta)$, and $k(f, \gamma)$. In the limit $k_i \gg \bar{k}(r)$, where the rate of interconversion between the states is much faster than the rate of transitioning to U, the ensemble of native states gets averaged out, acting as effectively a single state with net rupture rate $k(f) = p_\alpha k(f, \alpha) + p_\beta k(f, \beta) + p_\gamma k(f, \gamma)$. Here p_α is the stationary probability of the system being in state α . Since the interconversion rate is identical between all pairs of states, $p_\alpha = p_\beta = p_\gamma = 1/3$. If we choose rate functions such that $k(f, \alpha) = 3\tilde{k}(f, \alpha)$, and similarly for β and γ , we should find that the $\Omega_r(f)$ curves collapse to the same result as in the first, multiple pathway system. This is indeed what the numerical results in Fig. S4B show.

In contrast, if $k_i \ll \bar{k}(r)$, functional heterogeneity will manifest itself in the $\Omega_r(f)$ curves, and we get the non-collapse of Fig. S4C. Thus non-collapse is a signature of a particular kind of heterogeneity: multiple native states with slow rates of interconversion between them (i.e. due to high barriers separating the states). Such a system will by definition have many pathways to rupture (at least one from each native state), but the existence of multiple pathways is not by itself sufficient to trigger non-collapse.

The argument above has interesting implications for analyzing distributions of forces at which biomolecules fold (rather than unfold/rupture). These correspond to transitions starting in the unfolded ensemble, which should usually behave as a single state, having sufficiently fast interconversion times due to small energy barriers between unfolded configurations. Even if there were multiple pathways to fold to a single (or many) native states, the $\Omega_r(f)$ calculated

from the survival probability $\Sigma_r(f)$ of the unfolded state should exhibit collapse, assuming adiabaticity holds.

However, it is conceivable that the unfolded state ensemble in certain cases could be heterogeneous, partitioning into multiple states that do not interconvert readily. In this scenario, the refolding force distributions when analyzed using our theory would manifest heterogeneity. If this were the case then our framework offers an ideal way of investigating the nature of unbound complexes or unfolded states of proteins and RNA. These issues await future experiments.

4. DERIVATION OF NON-ADIABATIC SURVIVAL PROBABILITY

The derivation of Eq. (9) in the main text, the non-adiabatic limit of the survival probability $\Sigma_r(f)$ for the heterogeneous model, follows from an approach outlined by Hu, Cheng, and Berne [26]. This is closely related to the renewal method for calculating first-passage time distributions [45]. We are interested in $\Sigma_r(t)$, the probability that the system has never reached $x = x^\ddagger > 0$ at time t , given the initial condition $x = 0$ at $t = 0$. This yields $\Sigma_r(f)$ after the change of variables from t to $f(t) = rt$. In the model accounting for heterogeneity described in the main text, the value of b changes randomly with an interconversion rate k_i . However here we focus only on the case with no disorder, where x^\ddagger is fixed at a value of x_0^\ddagger .

The survival probability $\Sigma_r(t)$ can be expressed as an integral

$$\Sigma_r(t) = \int_{-\infty}^{x_0^\ddagger} dx P(x, t), \quad (S5)$$

where $P(x, t)$ is the probability that the particle is at x at time t , having never reached $x = x_0^\ddagger$ at any time prior to t . The initial condition is $P(x, 0) = \delta(x)$. Because of the $x = x_0^\ddagger$ condition, $P(x, t)$ is difficult to calculate directly, but it is related to the simpler Green's function $G(x, t|x', t')$ defined in the absence of any condition. $G(x, t|x', t')$ is just the probability of being at x at time t , given that it was at x' at time $t' \leq t$, and assuming the particle is allowed to diffuse in the $U(x, t) = (1/2)\omega_0 x^2 - rtx$ potential across the entire range $-\infty < x < \infty$. It satisfies the Fokker-Planck equation

$$\frac{\partial G}{\partial t} = D \frac{\partial}{\partial x} \left[e^{-\beta U(x, t)} \frac{\partial}{\partial x} \left(e^{\beta U(x, t)} G \right) \right], \quad (S6)$$

with initial condition $G(x, t'|x', t') = \delta(x - x')$. The connection between P and G arises from by noting that $G(x, t|0, 0)$ can be decomposed into two parts: (i) a contribution $P(x, t)$ from those trajectories that never reach x_0^\ddagger at any time prior to t ; (ii) a contribution from those trajectories that reach x_0^\ddagger for the first time at some $t' \leq t$, and then diffuse from x_0^\ddagger to x in the time $t - t'$. The distribution of first passage times to x_0^\ddagger is just $-d\Sigma_r(t)/dt$, and the probability of getting from x_0^\ddagger to x is $G(x, t|x_0^\ddagger, t')$. Putting everything together, we have

$$G(x, t|0, 0) = P(x, t) - \int_0^t dt' G(x, t|x_0^\ddagger, t') \frac{d\Sigma_r(t')}{dt'}. \quad (S7)$$

Solving Eq. (S7) for $P(x, t)$, and then integrating x from $-\infty$ to x_0^\ddagger , gives the following integral equation for $\Sigma_r(t)$ [26],

$$\Sigma_r(t) = \int_{-\infty}^{x_0^\ddagger} dx P(x, t) = \int_{-\infty}^{x_0^\ddagger} dx G(x, t|0, 0) + \int_0^t dt' \frac{d\Sigma_r(t')}{dt'} \int_{-\infty}^{x_0^\ddagger} dx G(x, t|x_0^\ddagger, t'). \quad (S8)$$

To make further progress, we note that the solution to Eq. (S6) for our choice of $U(x, t)$ is

$$G(x, t|x', t') = \frac{1}{\sqrt{2\pi\sigma(t-t')}} \exp\left(-\frac{(x - \mu(x', t-t'))^2}{2\sigma(t-t')}\right), \quad (S9)$$

$$\sigma(t) \equiv \frac{1 - e^{-2\beta D\omega_0 t}}{\beta\omega_0}, \quad \mu(x, t) \equiv \frac{r(\beta D\omega_0 t - 1) + e^{-\beta D\omega_0 t}(r + \beta D\omega_0^2 x)}{\beta D\omega_0^2},$$

for $t \geq t'$. This describes a Gaussian function with time-dependent mean μ and variance σ . In the limit $r \rightarrow \infty$ the mean μ rapidly increases with t , and the character of the dynamics becomes more ballistic than diffusive. As a result the contribution (ii) described above, from those trajectories that diffuse backward from x_0^\ddagger to some $x \leq x_0^\ddagger$, becomes

negligible. Thus $G(x, t|0, 0) \approx P(x, t)$ for $r \rightarrow \infty$, and we can approximate Eq. (S8) as

$$\begin{aligned} \Sigma_r(t) &\approx \int_{-\infty}^{x_0^\ddagger} dx G(x, t|0, 0) \\ &= \frac{1}{\sqrt{2\pi\sigma(t)}} \int_{-\infty}^{x_0^\ddagger} dx \exp\left(-\frac{(x - \mu(0, t))^2}{2\sigma(t)}\right) \\ &= \frac{1}{2} \left(1 + \operatorname{erf}\left[\frac{x_0^\ddagger - \mu(0, t)}{\sqrt{2\sigma(t)}}\right]\right) \end{aligned} \quad (\text{S10})$$

Plugging in the values of $\mu(0, t)$ and $\sigma(t)$ from Eq. (S9), and making the change of variables $f = rt$, gives the approximate expression for $\Sigma_r(f)$ in Eq. (9) of the main text.

5. SENSITIVITY OF THE HETEROGENEITY ANALYSIS TO EXPERIMENTAL ARTIFACTS

All five sets of experimental data that exhibited heterogeneity in Fig. 6 of the main text were collected using AFM pulling experiments. (In contrast three of the collapsed data sets in Fig. 5 were from optical tweezer studies, while the other two used AFM.) Thus it is important to check whether any aspects of the AFM experimental apparatus or procedure could influence the analysis of heterogeneity. We will consider three separate issues: cantilever force resolution and drag, noise due to finite sampling of the rupture distributions, and apparatus response time. We will focus on the AFM case, since this is most relevant to the existing data, but the discussion can easily be generalized to optical tweezers.

i) *Cantilever force resolution and drag*: AFM cantilevers typically have spring constants $\omega_c \sim \mathcal{O}(10 \text{ pN/nm})$. Thermal fluctuations of the cantilever limit the resolution at which forces can be measured to $\delta f \sim \sqrt{\omega_c k_B T}$, where for example $\delta f \sim 6 \text{ pN}$ when $\omega_c = 10 \text{ pN/nm}$ [46]. (Low-pass filtering of the data can in principle improve the force resolution [46, 47], but is not necessarily helpful for experiments involving steep force ramps, where maximum temporal resolution is necessary to pinpoint the rupture force.) The cantilever is also subject to viscous drag, with friction coefficient $\gamma(h)$ that in general depends on the geometry of the cantilever and its height h from the surface. Experimental measurements of this drag are often fit well by a phenomenological scaled spherical model, $\gamma(h) = 6\pi\eta a_{\text{eff}}^2/(h + h_{\text{eff}})$, where $\eta = 0.89 \text{ mPa}\cdot\text{s}$ is the viscosity of the surrounding water at room temperature, and a_{eff} and h_{eff} are parameters with dimensions of length [39, 40]. We will choose typical experimental values of $a_{\text{eff}} = 25 \text{ }\mu\text{m}$ and $h_{\text{eff}} = 5 \text{ }\mu\text{m}$, and assume that the rupture measurements are all conducted at $h \ll h_{\text{eff}}$, so in our analysis the drag coefficient is approximately constant, with a value $\gamma \approx 2 \text{ pN}\cdot\text{s}/\mu\text{m}$ (which matches the measured drag coefficient in Ref. [34]).

An unloaded (post-rupture) cantilever moving at fast pulling speeds of $v > 1 \text{ }\mu\text{m/s}$ (or ramp rates $r > 10^4 \text{ pN/s}$ for $\omega_c = 10 \text{ pN/nm}$) away from the surface will feel drag forces $f_{\text{drag}} = \gamma v > 2 \text{ pN}$. Since in experiments the magnitude of the rupture force is defined as the difference in the pre-rupture and post-rupture force levels, the drag creates a velocity-dependent artifact. The magnitude of the error in the measured rupture force depends also on velocity of the cantilever tip pre-rupture, and hence the stiffness of the sample: the softer the sample, the smaller the velocity difference of the tip pre- and post-rupture, and the smaller the error [39–41]. However in typical biomolecule rupture experiments the sample at the point of rupture is maximally extended, with large stiffness, and the tip velocity is much slower than the pulling velocity. In the limit where tip velocity immediately pre-rupture is zero, the error reaches its maximal value: the measured rupture force is approximately γv smaller than the actual one due to the drag offset post-rupture. This underestimation has been observed in fast AFM pulling experiments on the I27 domain of titin [40, 41].

To see the effects of cantilever artifacts on the heterogeneity analysis, we compared two different numerical approaches for the FBL model: a) The approach described in the main text and SI Sec. 2 (with results in Fig. 2 of the main text). The simulations have an idealized force ramp $f(t) = rt$ at fixed r with no cantilever artifacts. The rupture force in a simulation trajectory is just recorded as rt_{rup} , where t_{rup} is the time of rupture. b) An analogous approach, using the Hamiltonian $U(x, t) = (1/2)\omega_0 x^2 + (1/2)\omega_c(x_c(t) - x)^2$. Here $x_c(t)$ mimics the experimentally-controlled position of the clamped end of the cantilever, with the tip end-point assumed to be at x , and hence subject to thermal fluctuations. The cantilever stiffness is set to $\omega_c = 10 \text{ pN/nm}$. To achieve an average ramp rate of r , the position $x_c(t) = vt$, with the velocity chosen to be $v = r/\omega_c$. The rupture force for a simulation trajectory is recorded as $\omega_c(vt_{\text{rup}} - x_{\text{rup}}) - \gamma v$, where x_{rup} is the value of x at rupture, and the γv offset reflects the worse case scenario for drag-induced error.

Fig. S5 shows the numerical results for $\Omega_r(f)$ in the quenched disorder limit ($k_i = 0$) using the two approaches, with solid curves representing case a) and circles case b). Panels A through C correspond to different levels of disorder:

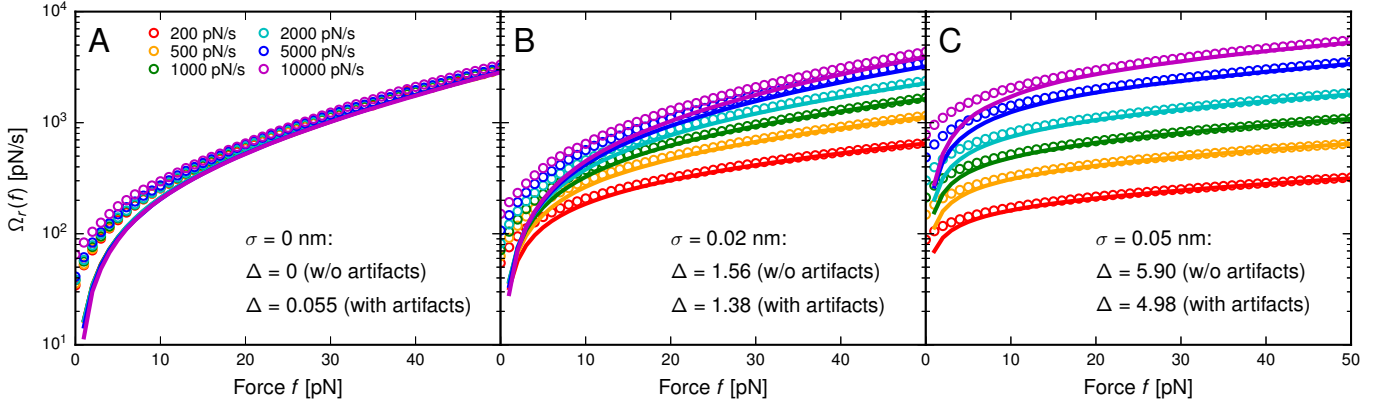


FIG. S5. Analysis of the FBL heterogeneous model system, using the two different numerical approaches described in SI Sec. 5.1. The parameters are the same as in Fig. 2 of the main text, and we show simulation results for three cases with $k_i = 0$: A) $\sigma = 0$ nm; B) $\sigma = 0.02$ nm; C) $\sigma = 0.05$ nm. The first numerical approach (solid curves) does not include cantilever artifacts, while the second (circles) does. The best-fit values of the heterogeneity parameter Δ from both approaches are listed in each panel.

$\sigma = 0, 0.02, 0.05$ nm, and in each panel the range of ramp rates is $r = 200 - 10000$ pN/s, comparable to the rates used in the experimental observations of heterogeneity (main text Fig. 6). The two numerical approaches converge as f increases, but show clear discrepancies in the low force regime ($\lesssim 10$ pN), a consequence of the cantilever artifacts. Despite these artifacts, the extracted heterogeneity parameters Δ from the two approaches are similar. In panel A ($\sigma = 0$ nm, no heterogeneity), we are close to total collapse even in the presence of artifacts, with a Δ value near zero. In panels B and C ($\sigma = 0.02$ and 0.05 nm) the Δ values of the second approach differ from the first one by less than 16% due to the artifacts. In all these cases there are sufficient data points at larger forces ($f \gtrsim 10$ pN) to mitigate the cantilever effects, and give a robust estimation of Δ . We note that all the experimental data sets in Fig. 6 of the main text entirely fall in this larger force regime, and thus should yield reliable values for Δ , even without correcting for drag artifacts. (Though in at least one of the studies, corresponding to panel A of Fig. 6, the researchers explicitly corrected for cantilever drag in measurements at pulling speeds of $v > 1 \mu\text{m/s}$ [34].)

ii) *Finite sampling*: Since $\Omega_r(f)$ depends on the survival probability distribution $\Sigma_r(f)$, the analysis of heterogeneity is sensitive to sampling noise in this distribution. In typical experiments the number of rupture events recorded at each r is $\sim \mathcal{O}(10^2)$, and thus it is useful to determine the uncertainty in the best-fit values of Δ due to the finite sampling of the distribution. To do this, we investigated every heterogeneous experimental system in Fig. 6 of the main text, and carried out the following procedure: the minimal model best-fit theoretical result for $\Omega_r(f)$ was used to determine an analytical form for the survival probability distribution $\Sigma_r(f) = \exp(-\Omega_r(f)/r)$ at each experimental value of r . We then generated 1000 synthetic experimental data sets, drawing N_{ev} values of the rupture force f from the cumulative distribution $1 - \Sigma_r(f)$ at every r through inverse transform sampling. The value of N_{ev} is listed for each experimental system in Table S1, and is based on the number of rupture events per pulling speed measured in that particular study. For each of the 1000 synthetic data sets, the best-fit value of Δ was extracted, and from the resulting distribution of Δ values we calculated 95% confidence intervals (also listed in Table S1). The confidence intervals all lie within roughly 30% of the original best-fit value of Δ in each system. This again reinforces the robustness of the experimental Δ values determined in the main text.

iii) *Apparatus response time*: To more accurately describe the experimental dynamics, the equilibration rate k_{eq} should reflect the overall relaxation time of the biomolecule plus apparatus (i.e. AFM cantilever). Depending on the details of the biological system, either the biomolecule or apparatus might be rate-limiting in determining k_{eq} . If for example the apparatus response is rate-limiting, and it makes k_{eq} small enough that either $\bar{k}(r) > k_{\text{eq}}$ or $k_c(r) > k_{\text{eq}}$, we would violate the adiabatic condition. The experimental consequences of this would be similar to the largest ramp rates shown in Fig. 4 of the main text, where we examined the non-adiabatic limit. There would be no collapse in the $\Omega_r(f)$ curves, but the qualitative behavior would be very different from the heterogeneous case: the non-adiabatic $\Omega_r(f)$ curves grow further and further apart as r is increased. For a given f the non-adiabatic $\Omega_r(f)$ curve decreases with increasing r , the opposite of the behavior in the heterogeneous case. However we see no evidence of non-adiabatic behavior in any of the experimental data sets in either Fig. 5 (non-heterogeneous) or Fig. 6 (heterogeneous) of the main text. This indicates that the respective instrument relaxation rates must all be larger than the lower bounds on k_{eq} shown in Fig. 5F and 6F. In the AFM case, the relaxation rate of a cantilever with stiffness ω_c and friction

System	N_{ev}	Δ	95% CI for Δ
ICAM1-LFA1 [34]	200 ¹	1.5	1.0 – 1.7
Ran-imp β [35]	375 ²	2.6	1.8 – 2.8
DNA oligomer [36]	300 ²	5.5	4.2 – 6.3
DNA-expG [22]	200 ¹	7.4	5.5 – 8.0
RNA-AtGRP8 [38]	225 ²	13.3	9.2 – 15.2

¹ In cases where the number of recorded rupture events is not specified in the study, we set $N_{\text{ev}} = 200$, a typical value.

² In cases where a range of N_{ev} was reported, we chose the mean value of the range.

TABLE S1. Analysis of finite sampling effects on the determination of Δ from the experimental data in Fig. 6 of the main text. N_{ev} is the number of rupture events at each ramp rate in the experimental study, Δ is the best-fit theoretical value for the heterogeneity parameter, and the last column shows the 95% confidence interval (CI) for Δ . The CI's are based on results from 1000 synthetic data sets, generated as described in SI Sec. 5.ii.

coefficient γ is ω_c/γ . Using typical values of $\omega_c = 10$ pN/nm and $\gamma = 2$ pN·s/ μm , we get $\omega_c/\gamma = 5000$ s⁻¹, which is indeed larger than the lower bounds depicted in the figures.

6. RELATIVE LIKELIHOOD ANALYSIS OF HETEROGENEOUS VS. PURE MODEL FITTING FOR EXPERIMENTAL DATA

As further validation of our heterogeneity analysis, we compared the likelihood $\mathcal{P}(\mathcal{D}|\mathcal{M})$ of obtaining the experimental data \mathcal{D} (the histograms for the rupture force distributions $p_r(f)$) given two choices of theoretical model \mathcal{M} :

1. *Heterogeneous model* \mathcal{M}_{het} : from Eqs. (6) and (7) in the main text, this model yields an analytical form for $\Omega_r(f)$ based on three parameters: Δ , k_0 , and x^\ddagger . The predicted rupture force distribution $p_r(f)$ is given by:

$$p_r(f) = -\frac{d\Sigma_r(f)}{df} = -\frac{d}{df} e^{-\Omega_r(f)/r} = \frac{k_0 e^{\beta f x^\ddagger}}{r} \left(1 + \frac{\Delta k_0 (e^{\beta f x^\ddagger} - 1)}{\beta r x^\ddagger} \right)^{-\frac{\Delta+1}{\Delta}} \quad (\text{S11})$$

2. *Pure model* $\mathcal{M}_{\text{pure}}$: this model assumes that we are pulling adiabatically on a system with a single functional state, with rupture described by the DHS [28] rate in Eq. (S3), which is the most widely used theoretical fitting form in the pure case. The predicted rupture force distribution $p_r(f)$ for this model is:

$$p_r(f) = \frac{k_0 \left(1 - \frac{\nu f x^\ddagger}{G^\ddagger} \right)^{-\frac{\nu-1}{\nu}}}{r} \exp \left[\beta G^\ddagger \left(1 - \left(1 - \frac{\nu f x^\ddagger}{G^\ddagger} \right)^{1/\nu} \right) + \frac{k_0}{\beta r x^\ddagger} \left(1 - e^{\beta G^\ddagger (1 - (1 - \nu f x^\ddagger / G^\ddagger)^{1/\nu})} \right) \right] \quad (\text{S12})$$

Setting $\nu = 2/3$ (the other choice $\nu = 1/2$ gives similar results) this model then depends on three fitting parameters: k_0 , x^\ddagger , and G^\ddagger . The DHS model reduces to the pure Bell theory when $G^\ddagger \rightarrow \infty$. Since the $\Delta \rightarrow 0$ limit of the heterogeneous model also yields the pure Bell theory, Eq. (S11) when $\Delta \rightarrow 0$ and Eq. (S12) when $G^\ddagger \rightarrow \infty$ are equivalent. Away from those limits, the two models give different results for $p_r(f)$.

For each experimental system, there are measurements from N^{load} different loading rates r_ρ , $\rho = 1, \dots, N^{\text{load}}$. The data at each loading rate are given as a set of N_ρ^{hist} histogram counts $\{f_{\rho,i}, N_{\rho,i}\}$, $i = 1, \dots, N_\rho^{\text{hist}}$, where $f_{\rho,i}$ is the force at which the i th bin is centered, and $N_{\rho,i}$ is the number of experimental trajectories which ended in rupture at a force f that fell within the bin range $f_{\rho,i} - w/2 < f < f_{\rho,i} + w/2$. Here w is the width of the bin. For any loading rate the total number of events is taken to be constant, $N_{\text{ev}} = \sum_i N_{\rho,i}$, with the values of N_{ev} for each experimental system we analyzed listed in Table S1. The assumption of constant N_{ev} is due to the fact that most studies did not explicitly list the individual values of $\sum_i N_{\rho,i}$ for each ρ , but instead gave a typical range. For a given model \mathcal{M} and

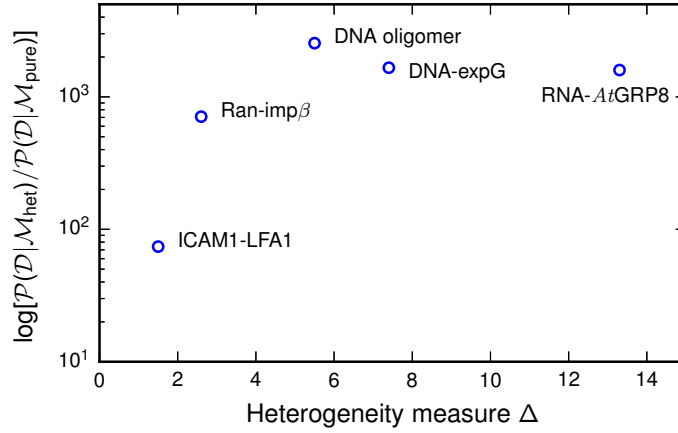


FIG. S6. The logarithm of the relative likelihood, $\log[\mathcal{P}(\mathcal{D}|\mathcal{M}_{\text{het}})/\mathcal{P}(\mathcal{D}|\mathcal{M}_{\text{pure}})]$ of the heterogeneous model versus the pure model for the experimental data from five studies: ICAM1-LFA1 [34], Ran-imp β [35], DNA oligomer [36], DNA-expG [22], RNA-AtGRP8 [38]. The log-relative-likelihood is plotted on the vertical axis, while the horizontal axis shows the corresponding results for the heterogeneity parameter Δ .

its corresponding set of parameter values, the probability of observing an experimental rupture outcome that falls within the $f_{\rho,i}$ bin is:

$$\mathcal{P}_{\rho,i}(\mathcal{M}) = \int_{f_{\rho,i}-w/2}^{f_{\rho,i}+w/2} df p_r(f) \quad (\text{S13})$$

with $p_r(f)$ given by either Eq. (S11) or (S12) depending on \mathcal{M} . The overall likelihood of all the experimental outcomes for a system is:

$$\mathcal{P}(\mathcal{D}|\mathcal{M}) = \prod_{\rho=1}^{N^{\text{load}}} \prod_{i=1}^{N_{\rho}^{\text{hist}}} [\mathcal{P}_{\rho,i}(\mathcal{M})]^{N_{\rho,i}} \quad (\text{S14})$$

The relative likelihood $\mathcal{P}(\mathcal{D}|\mathcal{M}_{\text{het}})/\mathcal{P}(\mathcal{D}|\mathcal{M}_{\text{pure}})$ is a measure of how much more likely it is that the heterogeneous model describes the experimental data compared to the pure model. Note that both models depend on the same number of parameters. The value of $\mathcal{P}(\mathcal{D}|\mathcal{M}_{\text{het}})$ for each experimental system with nonzero Δ is calculated using the parameters listed in Fig. 6 of the main text. For the pure model, we found the parameter set k_0 , x^{\ddagger} , and G^{\ddagger} that maximizes $\mathcal{P}(\mathcal{D}|\mathcal{M}_{\text{pure}})$ and used that maximum likelihood value for the comparison. In Fig. S6 we plot the logarithm of the relative likelihood, $\log[\mathcal{P}(\mathcal{D}|\mathcal{M}_{\text{het}})/\mathcal{P}(\mathcal{D}|\mathcal{M}_{\text{pure}})]$ on the vertical axis for the experimental systems, versus the corresponding value of the heterogeneity parameter Δ on the horizontal axis. All the relative likelihoods overwhelmingly favor the heterogeneous model. Even the smallest relative likelihood, which coincides with the smallest Δ value (ICAM1-LFA1 with $\Delta = 1.5$) is still highly favorable for heterogeneity, with a ratio $\mathcal{P}(\mathcal{D}|\mathcal{M}_{\text{het}})/\mathcal{P}(\mathcal{D}|\mathcal{M}_{\text{pure}}) \approx 10^{32}$. Thus we can conclude that for the systems identified as heterogeneous by their Δ values (corresponding to non-collapse of the $\Omega_r(f)$ curves), the best available pure model is an extremely unlikely alternative description. The collective data for each system, representing hundreds of experimental trials, unambiguously points to heterogeneity.